

COLOR FRINGE PROJECTION FOR 3-D TOPOGRAPHY

**DESIGN OF A COLOR FRINGE PROJECTION SYSTEM
FOR 3-D TOPOGRAPHY**

By

Clarence Wust, B.Sc.

A Thesis

**Submitted to the School of Graduate Studies
in Partial Fulfilment of the Requirements
for the Degree
Master of Engineering**

McMaster University

[C] Copyright by Clarence Wust

(February) 1990

ABSTRACT

Holography and projection Moire are well known techniques to obtain topographical information of a surface from a two dimensional image. Due to the image processing advances made in the area of computer vision these techniques are becoming more popular for machine vision inspection applications.

This thesis reviews the current holographic and projection Moire techniques and shows some of the practical limitations. Work was carried out to use techniques based on holography for machine vision applications. Through this work a novel idea was developed to resolve the topography of an object, making it more attractive for an industrial environment.

The idea is based on projecting three sinusoidal gratings, each being of a primary color, simultaneously onto a surface and recording the resulting intensity patterns with a color camera. Experimental results are presented which show the topographic contour of several objects.

ACKNOWLEDGEMENTS

The author wishes to express his sincere gratitude to his supervisors, Dr. Capson and Dr. Yellowley for their support and advice throughout the course of the research.

Appreciation is also extended to the Department of Engineering Physics who were always willing to be of assistance with topics related to optics.

The assistance of Paul Knowles of the Audio and Visual Department is also appreciated for giving me the opportunity to generate the required slides.

Finally, I want to thank my family for their love and understanding, especially my sister-in-law (and friend) Elly who kept my spirits up and fed me good nutritious meals on Sundays.

TABLE OF CONTENTS

	<u>PAGE</u>	
CHAPTER 1.	Introduction	1
CHAPTER 2.	Gaging Techniques in Metalworking	4
	2.1 Optical Gaging with Triangulation	5
	2.2 Confocal Optical Scanning Technique	6
	2.3 Interferometric Gaging Techniques	9
	2.3.1 Holography	9
	2.3.2 Projection Moire	23
	2.3.3 Fringe Projection Method	28
	2.4 Practical Considerations with Interferometric Techniques	30
CHAPTER 3.	Design of a Color Fringe Projection System for 3-D Topography	37
	3.1 Design Description and Operation	38
	3.2 Calibration Procedure	42
	3.2.1 Gamma Correction	44
	3.2.2 Spectral Response Calibration	46
	3.3 Boundary and Gradient Detection	47

	<u>PAGE</u>
CHAPTER 4. System Testing	52
4.1 Test Objects Selected	52
4.2 Processing Example	56
4.3 Experimental Results of Test Objects	60
4.4 Error Evaluation	66
CHAPTER 5. Discussion	69
5.1 Conclusions	70
5.2 Suggestions for Further Research	70
APPENDIX I. Holography	73
APPENDIX II. Heterodyne Interferometry	78
APPENDIX III. Projection Moire and Fringe Projection	81
APPENDIX IV. Fringe Shapes of Michelson Interferometer	85
APPENDIX V. Equipment Used	89
REFERENCES	90

LIST OF FIGURES

<u>FIGURE</u>		<u>PAGE</u>
2.1	Geometrical configuration for triangulation	5
2.2	Optical gaging system based on intensity ratio	7
2.3	Optical set-up for holographic recording	10
2.4	Phase measurement by synchronous detection	13
2.5	Phase measurement by convolution in frequency domain	15
2.6	Optical set-up for heterodyne interferometry	18
2.7	Phase measurement for heterodyne interferometry	19
2.8	Optical set-up for projection Moire	23
2.9	Shadow images due to the projection angle	27
2.10	Optical set-up for fringe projection method	28
2.11	Grating formation by division of wave-front	31
2.12	Sine wave grating of 0.01 and 0.06 cycles per unit	33
2.13	Intensity at a single point while phase stepping the grating from 0 to 360'	33
3.1	Block diagram of color fringe projection gaging system	39
3.2	Phase measurement flow chart	40

<u>FIGURE</u>		<u>PAGE</u>
3.3	Calibration set-up for color fringe projection method	43
3.4	Sine wave with and without gama correction	45
3.5	Original and equalized histograms	47
3.6	Function of computed difference signals	48
3.7	a) Phase plot under sampled b) Phase plot properly sampled	51
4.1	Obtained data of ball	56
4.2	Difference and phase plot of ball	57
4.3	Profile of ball and error plot	60
4.4	Profile and error distribution of turbine blades	65
4.5	Profile and error distribution of plane	68
5.1	Television-optical operational amplifier	70
I.i	Holographic recording set-up	74
I.ii	Off-axis reference beam formation	75
II.i	Heterodyne optical set-up	78
III.i	Fringe projection on surface	81
III.ii	Projection Moire set-up	83
IV.i	Principle set-up of Michelson Interferometer	85
IV.ii	Rays coming from mirror M1 and M2'	86

<u>TABLES</u>		<u>PAGE</u>
4.1	Characteristics of test objects	54
4.2	Error distribution of analytical objects	62
4.3	Error distribution of turbine blades	64
4.4	Relative standard deviation of test objects	66

<u>TEXT INSERTS</u>		<u>PAGE</u>
2.1	Modular Transfer Function	20
2.2	Laser Speckle	32
3.1	Unwrap algorithm for a raster scan	50
4.1	Chromatic Aberration	67

<u>PHOTOGRAPHS</u>		<u>PAGE</u>
1	Michelson Interferometer	
	Combined into Fringe Projection Concept	36
2	Test Objects	55
3	Color Grating Projected on Ball	59

1.0 Introduction

The importance of gaging in metalworking manufacturing is a need that is well established. Especially in mass production or assembly line set-ups, the need to produce parts within a certain tolerance is essential to guarantee interchangeability and automatic assembly.

Traditionally, inspectors are responsible for assuring that the individual parts are machined according to the engineering specifications and if not machined properly, take corrective action. Corrective action can range from a minor change in process parameters to actually changing the manufacturing process. Because of the limits of a human inspector, one can only provide sampling inspection. Thus, for example, only one out of a hundred items might be checked.

In recent years, flexible manufacturing cells have been introduced. In such an environment, it seems natural to implement inspection on a continuous basis to assure that a machined part meets tight tolerance constraints. To accomplish this, it is required that the gaging technique is automated. An automated gaging system could function as a major sensor to provide information for adaptive control strategies which

in effect assures on-line quality control. A typical application in such an environment would be "tool wear monitoring", where the wear of the edge of the cutting tool is determined and this information is used to adjust the parameters for the turning process or monitor the dimensions between certain edge boundaries of the work piece.

The objective of this research is to devise an automated gaging system which obtains a three dimensional map of the work piece and is robust enough to be used in an industrial environment, i.e. relatively immune to electrical noise and mechanical vibrations. Since spatial dimensions are mostly specified between edge boundaries, it is especially the edge contours which the gaging device must detect.

The principle of the gaging system described in this thesis is an optical gaging system based on interferometry, where a sinewave pattern of light is projected on the object of interest. This sinewave distribution is then read into the computer by a video camera and from the phase shift of this sinewave the depth of the object can be established. This technique is similar to holography but has the advantage that the resolution can be adjusted to suit the application.

Chapter 2 gives a survey of the types of optical gaging devices already in existence. Special attention is given to Moire and other interferometric techniques since these techniques are closely related to what has been done in this work. In Chapter 3 a new concept of optical gaging is introduced based on color fringe projection. The design and calibration of this new technique is also discussed. Test results of this optical gaging device are discussed in Chapter 4. Chapter 5 concludes the thesis with some general observations and suggestions regarding Color Fringe Projection.

2.0 Gaging Techniques in Metalworking

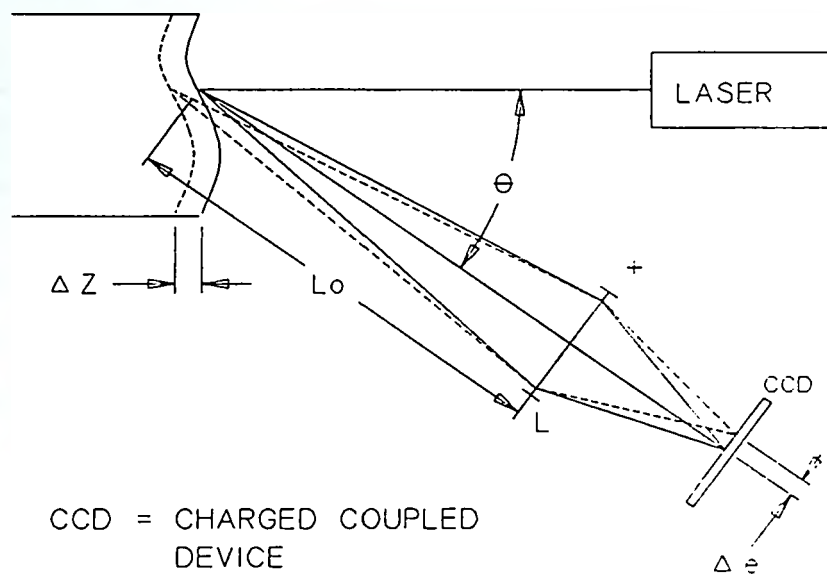
Conventional gaging techniques used in metalworking are extensive and the interested reader should consult specialized handbooks. Although automated gaging systems do exist, their uses are limited due to the fact that they are application sensitive. Pneumatic and electronic gaging systems are in use, but need to be tailored to the specific measurements one wants to make.

In recent years, due to the strong interest in computer vision, automated optical gaging systems have emerged which are more or less application independent. Numerous techniques have been proposed to obtain geometrical information. For a comprehensive review see [Besl, 88].

Two optical gaging systems, one based on triangulation and the second based on confocal scanning, will be discussed. These systems are very robust, but have the disadvantage that the geometrical information at only one point is evaluated. Systems based on interferometry, such as holography, Moire and fringe projection, do not have this restriction and will be discussed in greater detail in this Chapter.

2.1 Optical Gaging with Triangulation

Generally, the commercial systems available all evaluate only one geometrical¹ point of the object of interest. By measuring the properties of the reflected ray on the light sensor, the displacement can be calculated.



CCD = CHARGED COUPLED
DEVICE

L = LENS

Figure 2.1: Geometrical configuration for triangulation.

¹A point defined by the coordinates x, y and z .

A very robust way to measure a geometric point is by triangulation where a ray of light is projected under a known angle w.r.t. the light sensor. [Walters, 79]. By measuring the coordinates of the reflected ray, the geometric displacement can be calculated as:

(With reference to Figure 2.1)

$$L_0 \gg \Delta z \Rightarrow$$

$$\Delta e = \Delta z \sin\theta f / (L_0 - f)$$

where:

Δe = displacement of spot on sensor

Δz = surface displacement

θ = angle of projection

L_0 = working distance from lens to surface

f = focal length of lens

The advantage of this system is its inherent high signal to noise ratio. The intensity of the reflected ray can vary significantly without affecting the accuracy, since only the position of the ray has to be measured. The reported accuracy of such a system is about $2.5\mu\text{m}$.

2.2 Confocal Optical Scanning Technique

[Sawatari and Zipin, 79] describe an optical method of measuring the profile of an object similar to that of a

mechanical Proficorder¹. The principle of this instrument is shown in Figure 2.2.

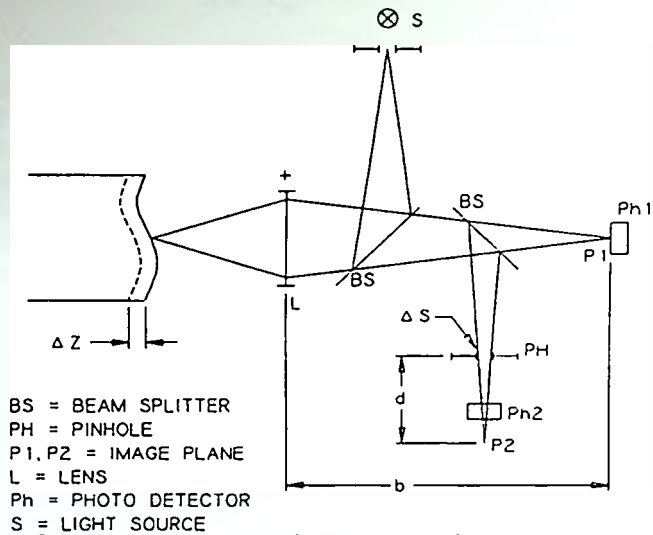


Figure 2.2: Optical gaging system based on intensity ratio.

Since the objective lens is used to illuminate the object and is used to focus the reflecting light, the name *Confocal* is appropriate. A light spot is projected on the contour to be measured while two photo detectors measure the reflection of the light spot reflected from the work piece. One detector (Ph1) measures the total intensity of the reflected rays while the second detector (Ph2) measures how much the light spot is out of focus. This is accomplished by placing a slit in front

¹A gaging device which uses a probe to touch the surface.

of detector Ph2. The displacement z , can now be computed as:

$$\frac{I_2(z) - I_2(0)}{I_1} = \frac{2 \Delta s (b-d) M^2 z}{\pi d^2 r_o}$$

Where:

- $I_2(z)$ = Intensity on Ph2 for a displacement z .
- $I_2(0)$ = Intensity at reference position.
- I_1 = Intensity on Ph1.
- Δs = slit width
- r_o = radius of lens L.
- M = lateral magnification of optical system.
- b, d = as shown in Figure 2.2.

Although the reported accuracy of this system is very good (about $0.3 \mu\text{m}$) the maximum allowed working distance is less than 1.5 mm. This requirement limits this device to be used with near coplanar surfaces only.

Both techniques discussed have the requirement for accurate servo systems to position the light ray or translate the work piece to obtain a contour of the surface. To avoid the need for such a servo system, one could observe the object of interest through a camera and determine the geometrical dimensions of the two dimensional plane seen by the camera. A well known approach to do this is through interferometry.

2.3 Interferometric Gaging Techniques

Interferometry is the result of two slightly different signals being superpositioned on each other. A typical example of interferometry in telecommunications would be a synchronous detector used for FM demodulation or in mechanical engineering, the use of a strobe light to detect the rotational speed of a shaft.

In optical engineering, interferometry is seen as the superposition of two or more electromagnetic (light) waves. As shown in this Chapter, holography is a form of interferometry while projection Moire and fringe projection are not. However, due to the strong mathematical similarities between the three techniques, in the literature they are usually grouped together.

2.3.1 Holography

Light reflected from an object is phase modulated by the geometric information of that object. The recording media presently known do not record this phase information but only the intensity of the light wave. In 1948 D. Gabor introduced

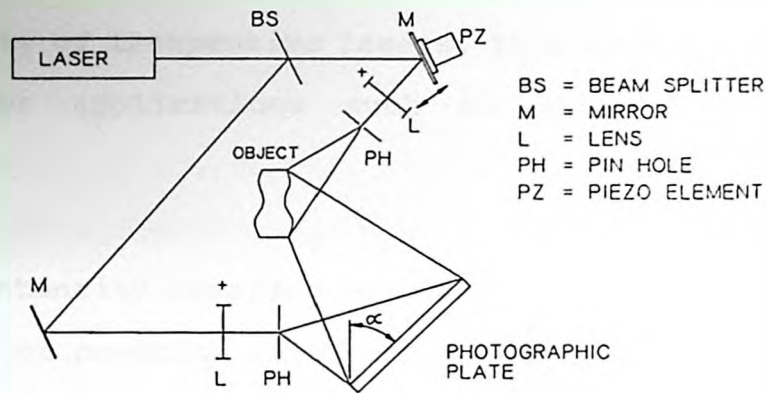


Figure 2.3: Optical set-up for holographic recording.

a novel idea to record this phase information by employing interferometry. By letting the light wave of the object interfere with a reference beam of light, coming from the same light source, the phase shifts introduced by the object are transformed to intensity variations on the recording plane. The optical set-up for holography is shown in Figure 2.3. On the recording medium, light is projected directly from the laser and from the object of interest. The light coming directly from the laser, the reference beam, will interfere with the light coming from the object and, as a result, the

geometrical information of the object is recorded through intensity modulation. Due to the advances in and wide availability of inexpensive lasers, this technique is now very popular for applications such as stress and structural analysis.

The intensity recorded over the two-dimensional plate as a function of position (x,y) is:

(See Appendix I for derivation.)

$$I(x,y) = E[a(x,y) + b(x,y) \cos(\phi r + \phi z + \delta)] \quad [2.1]$$

where:

$I(x,y)$ = intensity on the illuminated object
 E = proportional to the power of the laser
 $a(x,y)$ = irradiance of surface $0 \leq a(x,y) \leq 1$
 $b(x,y)$ = fringe visibility $0 \leq b(x,y) \leq 1$
 ϕr = $2\pi/\lambda \times \sin\alpha$
 ϕz = $2\pi/\lambda \times 2z$
 λ = wavelength laser light
 α = tilt
 z = displacement
 δ = introduced phase shift

This expression is generic in that the same form will be seen in projection Moire and fringe projection. It shows that the resulting intensity is composed of a bias intensity, namely the product of the laser power and the term $a(x,y)$, which is modulated by a sine wave signal proportional to the product of the laser power and the term $b(x,y)$. The "constants" $a(x,y)$ and $b(x,y)$ are a function of the surface of the object. The

term ϕ_z represents the displacement in the z direction of the object which is phase modulated on the carrier ϕ_r .

Several methods exist to solve equation 2.1 for finding ϕ_z and to resolve the geometrical position at a point (x,y). One could solve equation 2.1 directly, but this is not very practical since $a(x,y)$ and $b(x,y)$ are not known. Two approaches exist to solve for ϕ_z , namely methods based on a single wave front measurement and methods based on multiple wave front measurements. Techniques using a single wave front to solve for ϕ_z are:

- a) Synchronous detection.
- b) Convolution in frequency domain.

These methods have the advantage that the terms $a(x,y)$ and $b(x,y)$ need not be known, as will be seen from the discussion which follows.

Phase detection through synchronous detection:

Figure 2.4 gives the block schematic of solving for ϕ_z by synchronous detection from a single wave front. Synchronous detectors have been used in telecommunications systems for a long time; [Womack, 84] applied a Quadrature Carrier multiplexing system to find the phase shift ϕ_z from equation 2.1. He called this technique the Quadrature Multiplicative

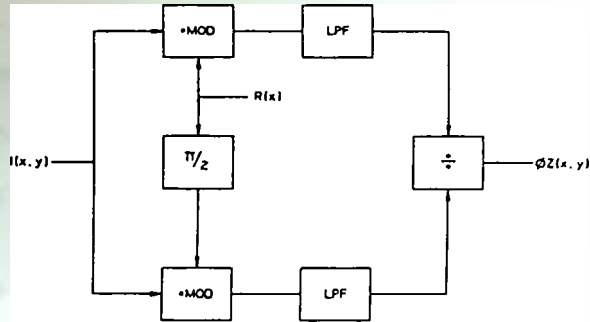


Figure 2.4:Phase measurement by synchronous detection.

Moire (QMM) algorithm. To understand the operation, equation 2.1 is rewritten as:

$$I(x,y) = A(x,y) + B(x,y) \cos (\phi_r + \phi_z)$$

where:

$$A(x,y) = E a(x,y)$$

$$B(x,y) = E b(x,y)$$

With a reference signal introduced as:

$$R(x,y) = \cos \phi_r$$

then the product of $I(x,y)$ and $R(x,y)$ is:

$$I(x,y) R(x,y) = A(x,y) \cos \phi_r + \frac{1}{2}B(x,y) \cos (\phi_r + \phi_z) + \frac{1}{2}B(x,y) \cos \phi_z$$

Putting this signal through a low pass filter leads to a signal of:

$$M1(x,y) = \frac{1}{2}B(x,y) \cos \phi z$$

Shifting the reference signal $R(x,y)$ over $\pi/2$ rads and again calculating the product between $I(x,y)$ and $R(x,y)$ after the low pass filter gives:

$$M2(x,y) = \frac{1}{2}B(x,y) \sin \phi z$$

The phase shift ϕz can now be found as:

$$\phi z = \text{atan}[M2(x,y)/M1(x,y)]$$

Phase detection through convolution in frequency domain:

A similar technique is based on performing a convolution in the frequency domain. [Takeda *et al*, 82] Equation 2.1 can be rewritten as:

$$I(x,y) = a(x,y) + c(x,y) \exp(j\phi r) + c^*(x,y) \exp(-j\phi r)$$

With:

$$c(x,y) = \frac{1}{2} b(x,y) \exp(j\phi z)$$

This approach is shown in Figure 2.5, where the FFT of equation 2.1 is taken and multiplied by an appropriate filter to bypass one of the side lobes.

By performing an Inverse Fourier transform, the phase shift can be found as:

$$\phi z = \text{atan}\{\text{Im}[c(x,y)]/\text{Re}[c(x,y)]\}$$

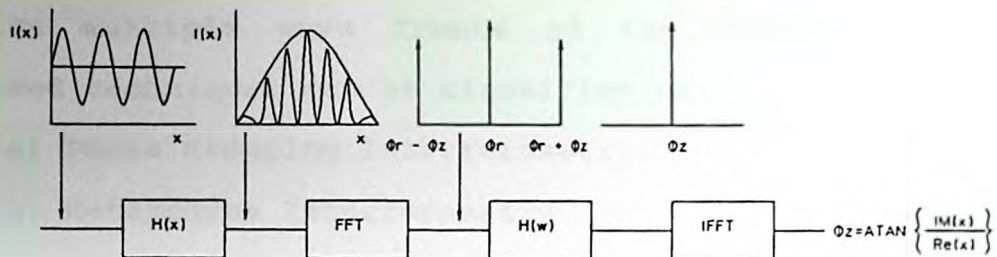


Figure 2.5:Phase measurement by convolution in frequency domain.

From the above discussion it is obvious that solving ϕz by QMM or convolution has some major drawbacks. Namely, unless some special hardware is used, the operations are very time consuming. An even more serious drawback is the need for filtering the data. With the QMM a low pass filter operation is required while for the FFT a Hanning filter operation must be performed to avoid ringing. Filtering the data means that the transients introduced by edges are affected. As stated in the introduction, this edge information is critical for gaging operations.

Techniques have been proposed to simultaneously preserve the edge information and simplify the calculation of the phase shift, resulting in faster algorithms. These algorithms

require multiple wave fronts of the interferogram. The proposed techniques can be classified as:

- a) Phase Stepping Interferometry.
- b) Heterodyne Interferometry.

Phase Stepping Interferometry:

A technique called phase stepping interferometry¹ is based on introducing a phase shift in the hologram by changing the optical length of one of the beams. This can be achieved by mounting one of the mirrors on a piezo actuator as shown in Figure 2.3. [Morgan, 82] described a method for solving equation 2.1 for ϕz using least squares estimation. This is done by reading the intensity $I(x,y,\delta)$ for several values of δ which are equally spaced, thus say $\delta=0, \pi/2, \pi$ and $3\pi/2$.

The penalty function is assumed to be:

$$Q = \sum_{k=1}^N \{ I_k - E[a(x,y) + b(x,y) \cos(\phi r + \phi z + 2\pi k/N)] \}^2$$

where:

N = sample points

I_k = k -th intensity sample

Minimizing Q w.r.t. $(\phi r + \phi z)$ leads to the solution for ϕz

¹Here the variable δ introduced in equation 2.1 is used to show this phase shift mathematically.

of:

$$\phi_z = \text{atan}\left(\left[\sum_{k=1}^N I_k \sin 2\pi k/n \right] \div \left[\sum_{k=1}^N I_k \cos 2\pi k/n \right] \right) - \phi_r$$

Assuming that $N=4$ gives:

$$\phi_z = \text{atan}\left((I_2 - I_4) \div (I_1 - I_3) \right) - \phi_r$$

[Wyant *et al*, 83] introduced a similar expression based on three images sampled at $\delta=\pi/4$, $3\pi/4$ and $5\pi/4$ which leads to:

$$\phi_z = \text{atan}\left((I_2 - I_3) \div (I_1 - I_2) \right) - \phi_r$$

[Greivenkamp, 84] gives a generalized solution for phase stepping techniques, showing that the method of Morgan and Wyant are special cases.

Heterodyne Interferometry:

Heterodyne interferometry is similar to phase stepping but instead of positioning δ at some distinct positions, δ is varied continuously between 0 and 2π . The method employed to do this is shown in Figure 2.6 [R. Thalmann *et al*, 1985]. By introducing a small frequency shift in one of the recording beams, one will observe that the grating frequency is "running" over the image plane. This frequency shift is accomplished by using Acoustic Optical Modulators.

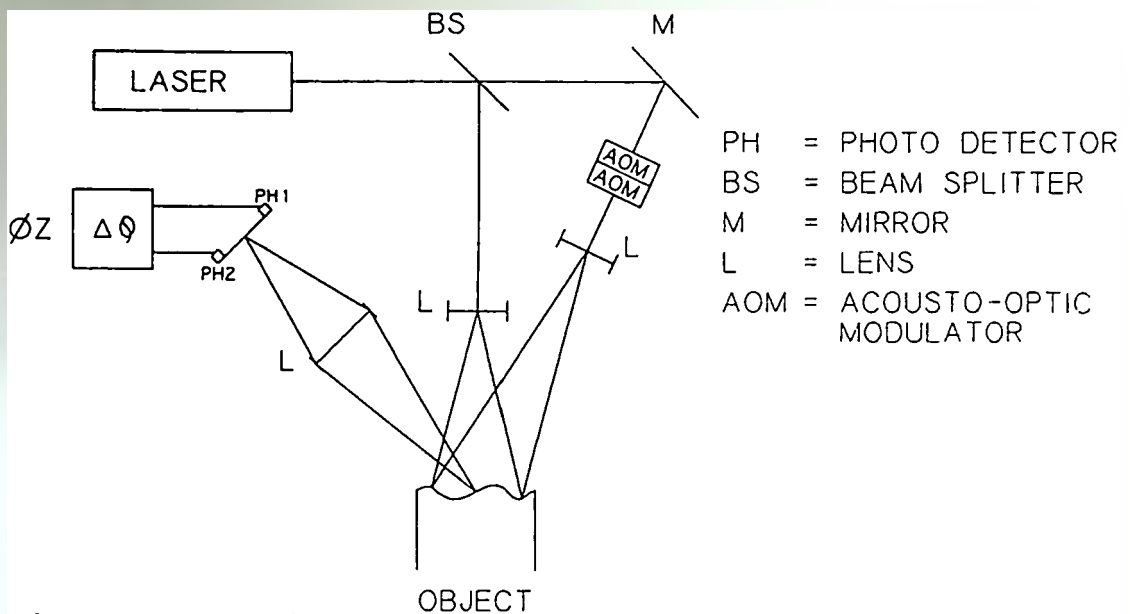


Figure 2.6: Optical set-up for heterodyne interferometry.

Under certain conditions, the intensity recorded by the photo detectors equals:

(see Appendix II for derivation)

$$I(x,y) = E^2 b(x,y) \cos(\Delta\omega t + \phi z)$$

By monitoring a point (x,y) w.r.t. a reference point, the phase shift ϕz can be found with common phase meters. Figure 2.7 shows such a system where the intensities $I_r(x)$ and $I(x)$ are the signals from photo detector 1 and 2 shown in Figure 2.6. If designed properly, this technique is very powerful

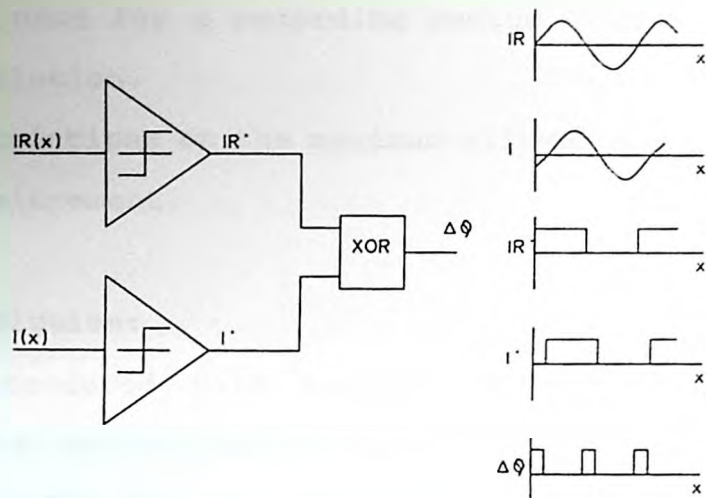


Figure 2.7:Phase measurement for heterodyne interferometry.

because of its high signal to noise ratio and the simplicity to measure the phase shift. Unfortunately, because of the relatively high bandwidth required for the image detector, it is not possible to use general video equipment.

As mentioned before, holography is well established in stress and structural analysis. However, it has certain restrictions which makes it unattractive for a general purpose gaging system.

These disadvantages can be grouped as:

- a) The need for a recording medium with a high spatial resolution.
- b) Restrictions on the maximum allowed discontinuity for displacement.

Spatial resolution:

The introduced tilt between the reference and the object wave is essential for all the methods discussed to calculate the phase shift. The maximum required tilt is related to the Modular Transfer Function (see insert) of the recording medium. From the sampling theorem it is known that to reconstruct a sampled signal, the sampling frequency must be two times the highest frequency in the sampled signal. Thus there is a minimum required MTF if the tilt is fixed. Referring back to equation 2.1, the carrier ϕ_r is given as:

$$\phi_r = 2\pi/\lambda \times \sin\alpha$$

which can be rewritten as:

$$\phi_r = 2\pi fg \times$$

where,

The Modular Transfer Function (MTF) can be seen as the bandwidth of the optical recording medium, mostly expressed in lines/mm. For a reference see [Goodman, 68] pg 114.

Insert 2.1: Modular Transfer Function.

$$fg = \text{grating frequency} = \sin\alpha/\lambda$$

The lowest grating frequency is obtained when $\alpha = \frac{1}{2}\pi$ for example, for a He-Ne laser with a wavelength of about $0.6\mu\text{m}$, the required MTF must be higher than:

$$\text{MTF} \geq fg/2 = \sin \alpha/2\lambda = 833 \text{ lines/mm}$$

To use a camera to record the holographic image is not very economical because of the high MTF required. Assuming a camera with 512 pixels per line, it would give a field of view of only 0.6mm with the stated MTF of 833 lines/mm.

Allowed Discontinuity:

As follows from the above discussion, it is the phase shift ϕz which is determined instead of the actual deformation z . Since the phase shift wraps around after 2π rads, the maximum discontinuity which can be measured is: (using equation 2.1)

$$\Delta z = \phi z \lambda/4\pi \Rightarrow \Delta z_{\text{max}} = \frac{1}{2} \lambda$$

Assuming again a He-Ne, with a wavelength of $0.6\mu\text{m}$, the maximum measurable discontinuity is $0.3\mu\text{m}$.

Considering the requirement for a recording medium with a high MTF, and the high sensitivity for displacement, holography becomes attractive only in certain applications where minute differences have to be detected. To overcome

these restrictions, especially that of the high sensitivity for displacement, projection Moire and fringe projection give an alternative.

2.3.2 Projection Moire

With projection Moire, a Ronchi¹ grating is projected onto the surface of interest while the image sensor records the scene through another Ronchi grating of the same frequency.

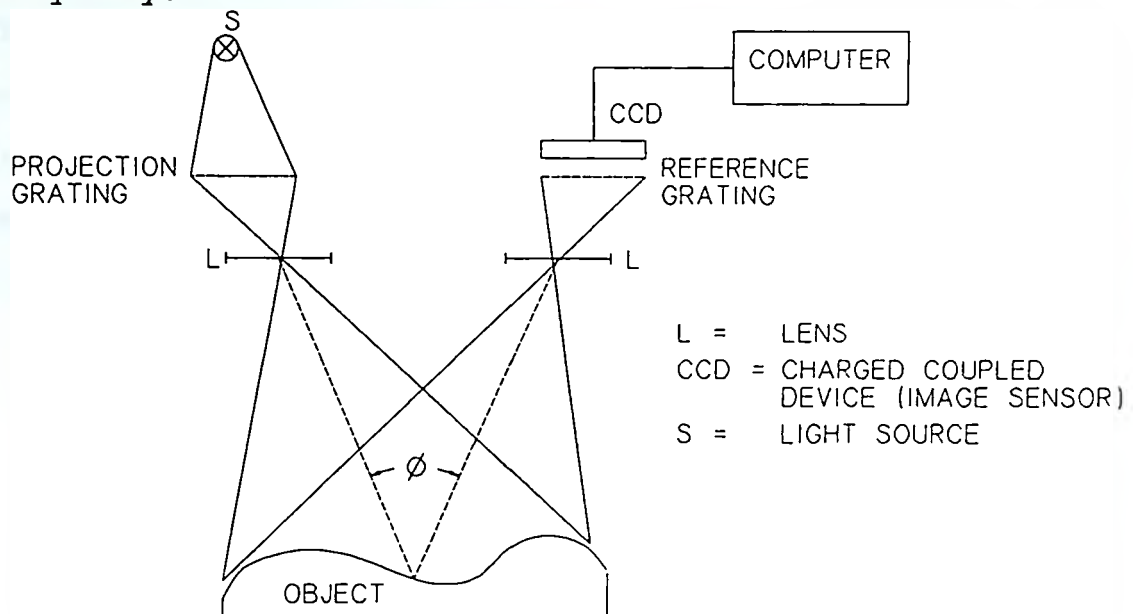


Figure 2.8: Optical set-up for projection Moire.

The grating in front of the camera is referred to as the reference grating. Figure 2.8 shows this set-up. The projected Ronchi grating will be phase modulated by the deformation of

¹Transparency with black bars on neutral background.

the surface and assuming only the first harmonic of the Ronchi grating, can mathematically be expressed as equation 2.1, with:

(see Appendix III for derivation)

$$\begin{aligned}\phi_r &= 2\pi/p \quad x \cos \theta \\ \phi_z &= 2\pi/p \quad z \sin \theta \\ p &= \text{period of grating} \\ \theta &= \text{projection angle (see Figure 2.8)}\end{aligned}$$

The intensity recorded on the CCD image sensor is now the product of the two transmittance functions of the gratings. As shown in Appendix III, the intensity recorded by the image sensor, assuming only first harmonics, is composed out of high frequency terms and by the deformation of the surface.

$$\begin{aligned}I(x,y) = E [&a(x,y) + a(x,y)\cos(\phi_r + \delta_r) + \\ &b(x,y)\cos(\phi_r + \phi_z + \delta_p) + \\ &\frac{1}{2}b(x,y)\cos(2\phi_r + \phi_z + \delta_p + \delta_r) + \\ &\frac{1}{2}b(x,y)\cos(\phi_z + \delta_p - \delta_r)] \quad [2.2]\end{aligned}$$

where:

$$\begin{aligned}I(x,y) &= \text{intensity on the illuminated object} \\ E &= \text{proportional to the light source} \\ a(x,y) &= \text{irradiance of surface } 0 \leq a(x,y) \leq 1 \\ b(x,y) &= \text{fringe visibility on surface } 0 \leq b(x,y) \leq 1 \\ \delta_r &= \text{phase shift in reference grating} \\ \delta_p &= \text{phase shift in projected grating} \\ \phi_r &= 2\pi/p \quad x \cos \theta \\ \phi_z &= 2\pi/p \quad z \sin \theta \\ \theta &= \text{angle of projection} \\ p &= \text{period of Ronchi grating}\end{aligned}$$

With projection Moire, a common technique used for determining ϕ_z is fringe counting. This technique is based on first

putting equation 2.2 through a low pass filter¹, which leads to:

$$I(x,y) = E [a(x,y) + \frac{1}{2}b(x,y)\cos(\phi z + \delta p + \delta r)] \quad [2.3]$$

Assuming $\delta p = \delta r$, equation 2.3 will have a minimum value each time ϕz equals π or 3π . Thus one could find the geometrical information in steps of Δz . In many applications of projection Moire such a coarse approach is satisfactory. If one needs a higher degree of resolution then equation 2.2 must be solved with algorithms similar to those used with holography.

Although not for a single wave front, the QMM method could be used to solve for ϕz by obtaining two images, one with $\delta r = \delta p$ and one with $\delta r = \frac{1}{2}\pi + \delta p$. Putting the images through a low pass filter to remove the higher frequencies will lead to:

$$\begin{aligned} M1(x,y) &= E [a(x,y) + \frac{1}{2}b(x,y)\cos(\phi z)] \\ M2(x,y) &= E [a(x,y) + \frac{1}{2}b(x,y)\cos(\phi z + \frac{1}{2}\pi)] \end{aligned}$$

The phase shift is then:

$$\phi z = \text{atan}\{M2(x,y) \div M1(x,y)\}$$

If the grating is sinusoidal, a phase stepping technique as shown by Morgan and Wyant can be used by moving δr or δp in four or three different positions respectively. The advantage of using one of these methods is that the higher frequencies

¹In practice this low pass filter is introduced by adjusting the lens so that the recorded image is slightly out of focus.

in equation 2.2 are automatically filtered out while edge information is retained. [Reid *et al*, 84]

[Halioua *et al*, 83] describe an approach similar to heterodyne interferometry. They suggest a system where the projection and reference grating are moved continuously while the recorded intensity is integrated w.r.t. time. The resulting intensity pattern is as of equation 2.3. The advantage of this approach is that edge information is preserved and the grating can be any periodic function. Thus a Ronchi grating can be used while still obtaining a precise contour image.

As with holography, the phase shift ϕz is measured instead of the displacement z . Now, the maximum discontinuity for z equals:

$$\Delta z = \phi z \frac{p}{2\pi \sin\theta} \Rightarrow \Delta z_{\max} = p/\sin \theta$$

Thus by changing the grating period or the projection angle, the maximum allowed discontinuity can be varied to fit the application. The reported maximum sensitivity for this method is about 0.1mm.

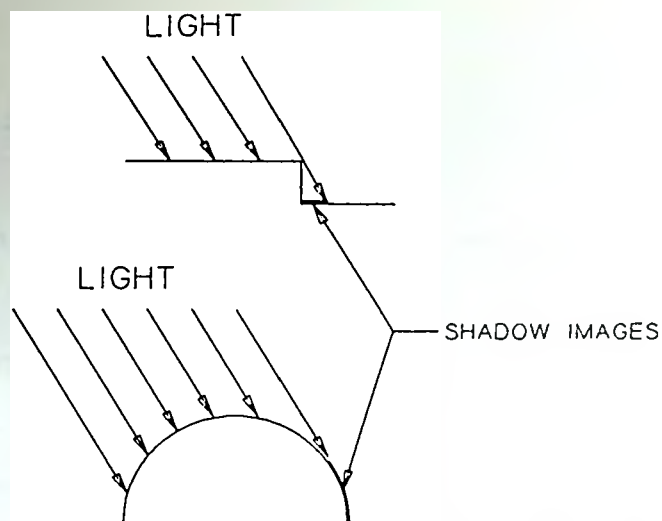


Figure 2.9:Shadow images due to the projection angle.

By introducing the projection angle θ , which is required to get information about the z displacement, the field of view of the camera is restricted by shadow images on the object of interest. For example in Figure 2.9 some cases are shown where the camera does not obtain all the geometrical data because of the angle of projection.

2.3.3 Fringe Projection Method

The fringe projection method discussed in this section is similar to that of holography. With holography, the maximum allowed discontinuity is proportional to half the wavelength of the laser. As stated in section 2.3.1, this results in a maximum discontinuity of $0.3 \mu\text{m}$ if a He-Ne laser is used. A versatile method to increase this allowed discontinuity is by

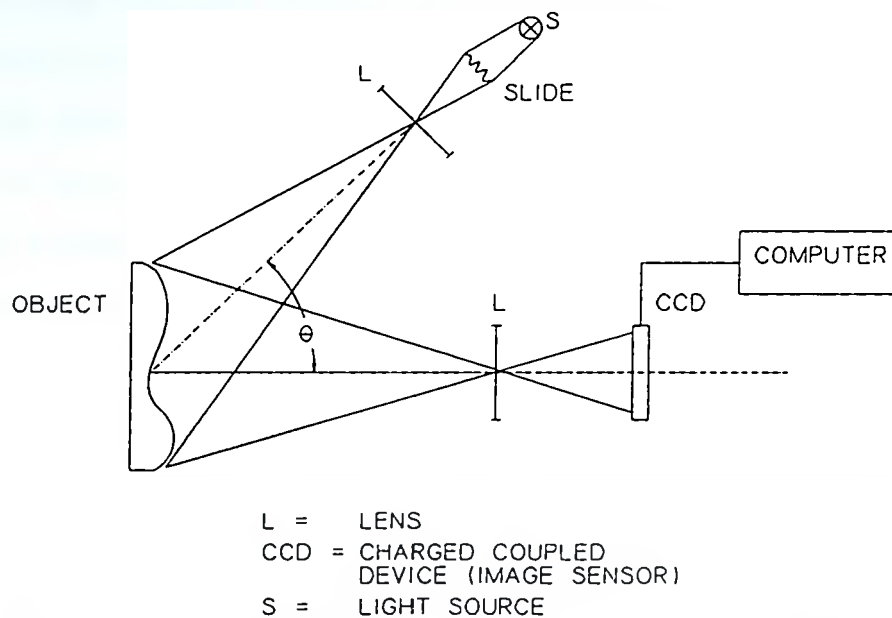


Figure 2.10: Optical set-up for fringe projection method.

employing a fringe projection method as discussed by [Dessus and Leblanc, 73]. With this method, a sinusoidal intensity

pattern is projected on the object as shown in Figure 2.10.

The resulting intensity pattern on the object is of the form:

$$I(x,y) = E[a(x,y) + b(x,y) \cos(\phi_r + \phi_z + \delta)] \quad [2.4]$$

Where:

$I(x,y)$ = intensity on the illuminated object

E = proportional to the power of light source

$a(x,y)$ = irradiance of surface $0 \leq a(x,y) \leq 1$

$b(x,y)$ = fringe visibility $0 \leq b(x,y) \leq 1$

ϕ_r = $2\pi/p \times \cos\theta$

ϕ_z = $2\pi/p \times z \sin\theta$

p = period of projected grating

θ = angle of projection

δ = introduced phase shift

The maximum allowed discontinuity can be changed by using a sinusoidal intensity pattern with a longer period, or by changing the projection angle. From Figure 2.10 it is clear that the optical set-up is also considerably more simple than that of holography or projection Moire. Furthermore the phase shift ϕ_z is much more easily calculated than with projection Moire.

2.4 Practical Considerations with Interferometric Techniques

From the review given in the previous sections, it is clear that the fringe projection method is preferred as a method for optical gaging for the following reasons:

- a) With respect to holography, the maximum allowed discontinuity can be adjusted by using a different grating period or change the angle of projection.
- b) Compared to projection Moire, solving for ϕz can be done in a simple manner.
- c) The optical set-up is the least complicated.

In this section a discussion is presented of the difficulties encountered by employing the fringe projection technique combined with a Michelson Interferometer to form the sine wave grating. As will follow from the discussion, the need for a servo system to position the grating and the use of a coherent light source are things one would like to avoid in a practical gaging set-up.

Figure 2.11 shows the principle set-up of a Michelson Interferometer. A polarized laser beam enters the interferometer and gets divided in amplitude by the beam

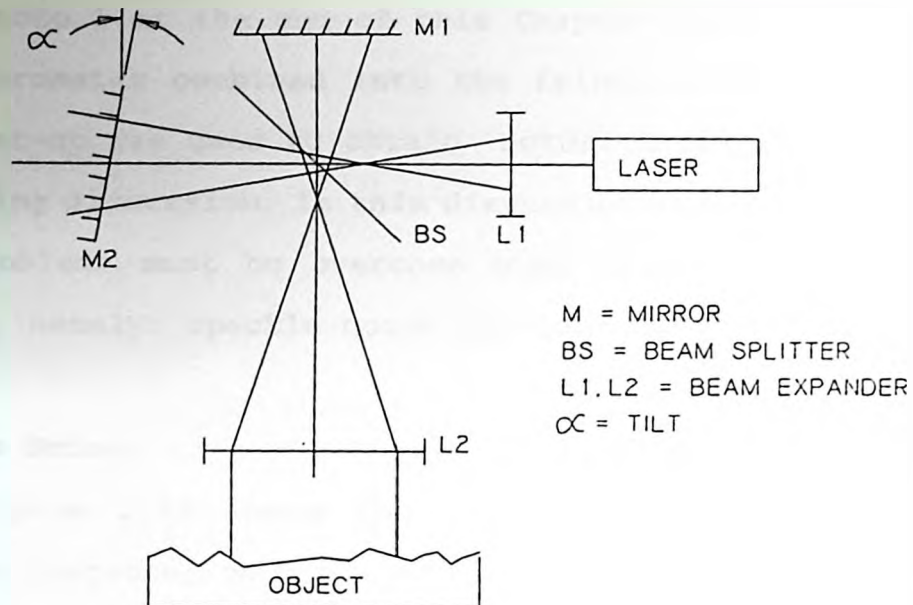


Figure 2.11: Grating formation by division of wave-front.

splitter which is mounted 45 degrees w.r.t. the laser beam. The two beams meet mirrors at practically normal incidence, return to the beam splitter and recombine. Since the beam splitter is 50% transmitting and 50% reflecting, the two exit beams, coming from the mirrors, have equal intensity. The total intensity leaving the interferometer is half of the original laser beam intensity. By tilting one of the mirrors, the exit beams will have an angle w.r.t. each other which will result in a sinusoidal intensity grating when they collide on a surface.

(See Appendix IV for the mathematical proof.)

Photo 1 at the end of this Chapter shows the Michelson Interferometer combined into the fringe projection concept. This set-up was used to obtain actual data presented in the following discussion. In this discussion it will be shown that two problems must be overcome when using a coherent light source, namely; speckle noise and laser instability.

Speckle Noise:

Figure 2.12 shows the intensity distribution of the grating projected on the a metallic surface for two different grating frequencies. The great amount of noise superimposed on the grating frequency is due to a phenomenon called speckle¹. Although this speckle noise reduces the Signal to Noise ratio of the grating, the effect can be strongly reduced, by employing phase stepping techniques. This is demonstrated in Figure 2.13 where the intensity at one point (x,y) is recorded while moving the

Speckle is the grainy structure of coherent light which is seen when projected on a surface. This speckle is dependent on the surface roughness and the angle of projection and can be used to study deformation of a surface [Hariharan, 85]. In this application it can be regarded as noise.

Insert 2.2: Laser Speckle

¹The noise introduced by the camera and frame grabber are not significant.

grating from 0 to 360 degrees.

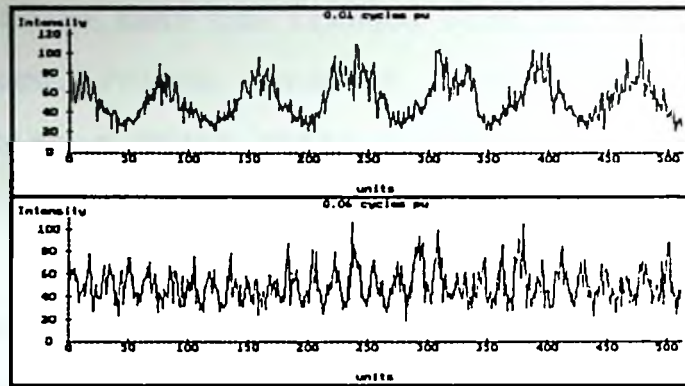


Figure 2.12: Sine wave grating of 0.01 and 0.06 cycles per unit.

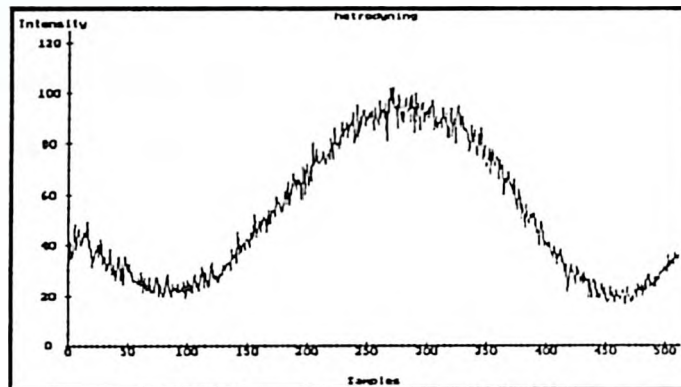


Figure 2.13: Intensity at a single point while phase stepping the grating from 0 to 360'.

Laser Instability:

A major problem observed with the Michelson Interferometer is that the fringes were moving w.r.t. a fixed point in space. Fringe movement is not desirable since it would appear as a phase shift w.r.t. the reference grating ϕ_r .

Fringe movement can be caused by:

- 1) vibrations of the work station.
- 2) changes in the breaking index of air.
- 3) instability of the laser.

It was concluded that the major cause of the fringe movement was due to laser instability. When the laser is cold the fringes are stationary while after the laser is in operation for about 5 minutes, the fringe movement begins. With laser instability the exit beam of the laser is not of a consistent wavelength but rather fluctuates. Although the laser is designed to oscillate for only one axial mode, the output frequency of the laser has a bandwidth of the order of 1 kHz. For a properly designed laser. Over a long time the frequency drift is even greater due to thermal and mechanical effects. This laser instability is very hard to correct since it requires that the cavity length, which determines the laser

resonant frequency, be controlled. Although systems do exist, [Hariharan, 85], it is not practical implementation in a gaging system.

Given the problems observed including the need for a servo system, speckle noise and especially the laser instability, it is apparent that a more robust technique is required, for practical implementation of a gaging system in an industrial environment.

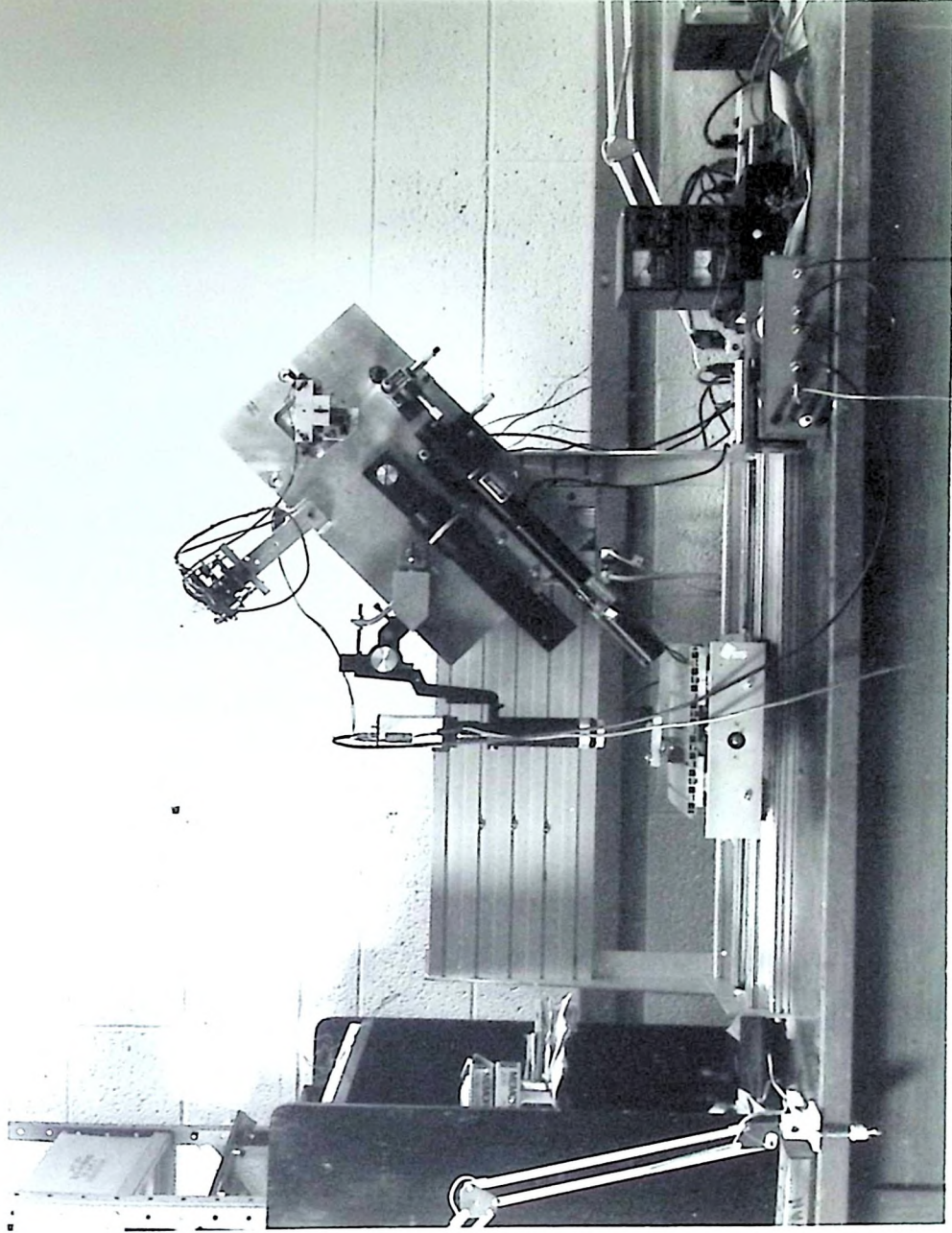


Photo 1: Michelson Interferometer
Combined into Fringe Projection Concept.

3.0 Design of a Color Fringe Projection System for 3-D Topography

From the discussion presented in the previous chapter, it is apparent that a gaging system based on using a laser to form a sinusoidal grating is not practical if one wants to use the gaging system in an industrial environment. To circumvent the need for a coherent light source, fringe projection can be employed.

To avoid the need for a servo system and still keep the calculation procedure to obtain ϕz simple, a color fringe projection technique is proposed. With the color fringe projection method, a photographic slide is generated with three sinusoidal gratings, each being of one of the primary colors, shifted 90 degrees apart. In essence this is still equivalent to phase stepping interferometry but instead of positioning the grating in different positions with a servo system, the grating positions are given different colors. By viewing the wave front with a color camera, the three individual images, namely the red, green and blue, are simultaneously known.

The idea of using color to determine the contour of an object has also been proposed by [Boyer and Kak, 87]. They projected strips of different colors onto an object and through triangulation determined the depth. This technique requires a cross correlation process to locate a certain color of strip in the image which, unless parallel processing is applied, is very time consuming. The proposed idea in this thesis is different in that a sinusoidal intensity pattern of colors is projected on the object, instead of strips, which simplifies the calculation procedure to find the contour. Photo 3 in Chapter 4 shows the three sinusoidal intensity patterns of colors projected on a ball.

3.1 Design Description and Operation

Figure 3.1 shows the overall block schematic of the gaging device. The slide is projected on the object with a commercial slide projector, while a three chip CCD camera reads the wave front of the object. The video amplifier has a computer controlled gain and offset adjust to control the spectral response of the red, green and blue color sensors. Since a B/W frame grabber is used in this experimental set-up, the color video signals are multiplexed into the frame grabber.

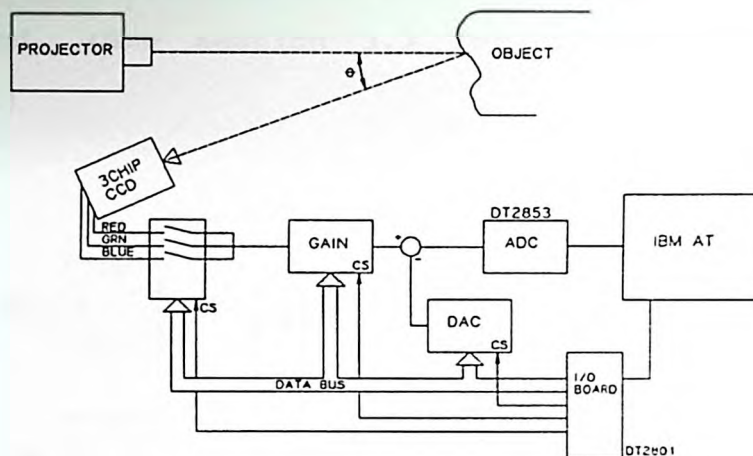


Figure 3.1: Block diagram of color fringe projection gaging system.

The projected light intensities are:

$$\begin{aligned}
 I_r(x,y) &= E_r[a(x,y) + b(x,y) \cos(\phi_r + \phi_z + \pi/4)] \\
 I_g(x,y) &= E_g[a(x,y) + b(x,y) \cos(\phi_r + \phi_z + 3\pi/4)] \\
 I_b(x,y) &= E_b[a(x,y) + b(x,y) \cos(\phi_r + \phi_z + 5\pi/4)]
 \end{aligned}
 \quad [3.1]$$

where:

$I(x,y)$ = intensity on the illuminated object
 E = proportional to the power of projector light
 $a(x,y)$ = irradiance of surface $0 \leq a(x,y) \leq 1$
 $b(x,y)$ = fringe visibility $0 \leq b(x,y) \leq 1$
 ϕ_r = $2\pi/p \times x \cos\theta$
 ϕ_z = $2\pi/p \times z \sin\theta$
 p = period of projected grating
 θ = angle of projection
 subscripts r,g,b; red, green and blue respectively.

The calculation procedure used to solve for $\phi_r + \phi_z$ is identical to that proposed by [Wyant *et al*, 83] and is shown in Figure 3.2. Knowing ϕ_r , the phase shift ϕ_z and thus the displacement z is found. (See section 3.3 for a discussion on this procedure.)

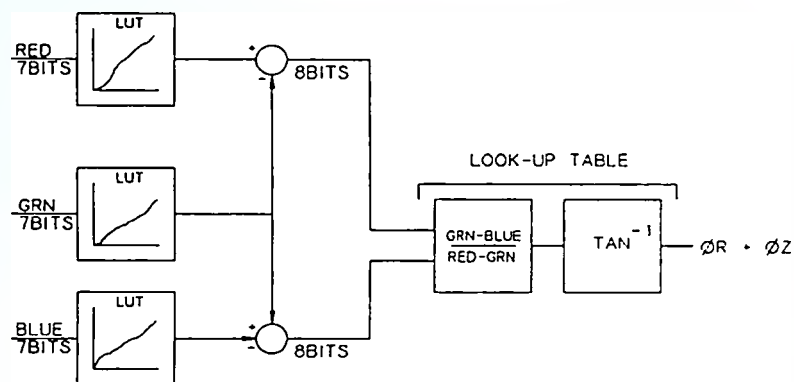


Figure 3.2: Phase measurement flow chart.

The production of the required color slides is facilitated by the recent advances made in computer graphics equipment. The slides used in this thesis were made by the Audio Visual Department of McMaster University with a matrix color camera. This camera can produce slides of 4000 by 3000 pixels on a 35mm slide.

To project the slide on the object and read it with the three chip CCD camera, it was found that the best spectral response was obtained by putting a 5400K color filter in front of the projector and a 3200K color filter in front of the camera.

3.2 Calibration Procedures

The proposed technique requires that the spectral response of the overall system must be flat i.e. the visibility of the red, green and blue wave fronts must be identical. Furthermore, the non-linear response of the camera must be compensated for.

To calibrate the overall optical and electronic system, a flat plane is put in front of the camera as shown in Figure 3.3. For good calibration results, this plane should cover the total field of view of the camera. The color fringes are projected on this plane and the camera system is ready for calibration.

The calibration procedure needs to be performed only once for a given optical set-up, assuming that the color of the measured object is the same as that of the calibration plane. Two points are addressed in this procedure, namely the non-linear response or gamma correction of the camera and the spectral response of the system.

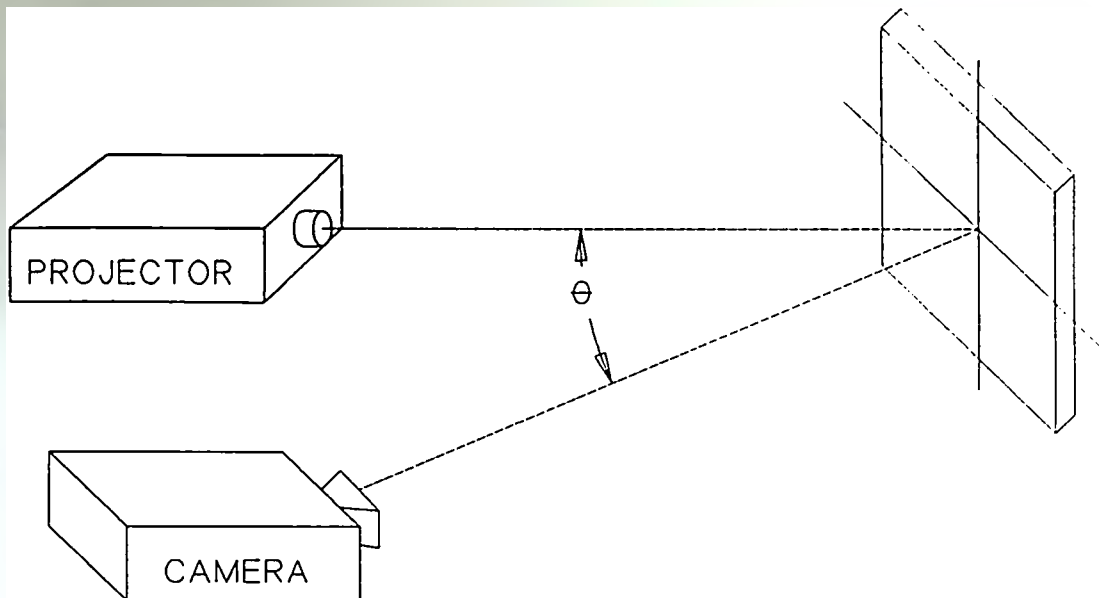


Figure 3.3: Calibration set-up for color fringe projection method.

The colored fringes are projected on the calibration plane while the gain and offset of the three video signals are adjusted such that the dynamic range of the red, green and blue video signals are similar. These adjustments are made manually through a computer interface. It is not required that the three signal amplitudes are exactly the same, since this will be done later through automated calibration routines. Once the hardware settings are fixed, the system is fine-tuned through software by adjusting the input look-up tables.

3.2.1 Gamma Correction

Due to the log linear response of the CCD image sensors, the recorded intensity versus the actual intensity equals:

$$I_v = G I^\gamma \quad [3.2]$$

where:

I_v = recorded video intensity by image sensor
 G = proportional constant
 I = actual intensity of object
 γ = sensitivity of image sensor

In the literature the sensitivity γ is frequently referred to as the "gamma" of the image sensor. For CCD image sensors this gamma is assumed to be unity, however, for low light levels this is not the case.

To compensate for the non-linear response of the image sensor, the inverse function of equation 3.1 must be found. Thus:

$$I = F(I_v) \quad [3.3]$$

Series compensation can be employed by programming $F(I_v)$ into the input look-up tables of the frame grabber. To find $F(I_v)$,

a slide with the fringe sine wave function is projected onto the calibration plane. Knowing that the histogram of a sine wave must be flat, applying histogram equalization on the obtained image will give the required function.

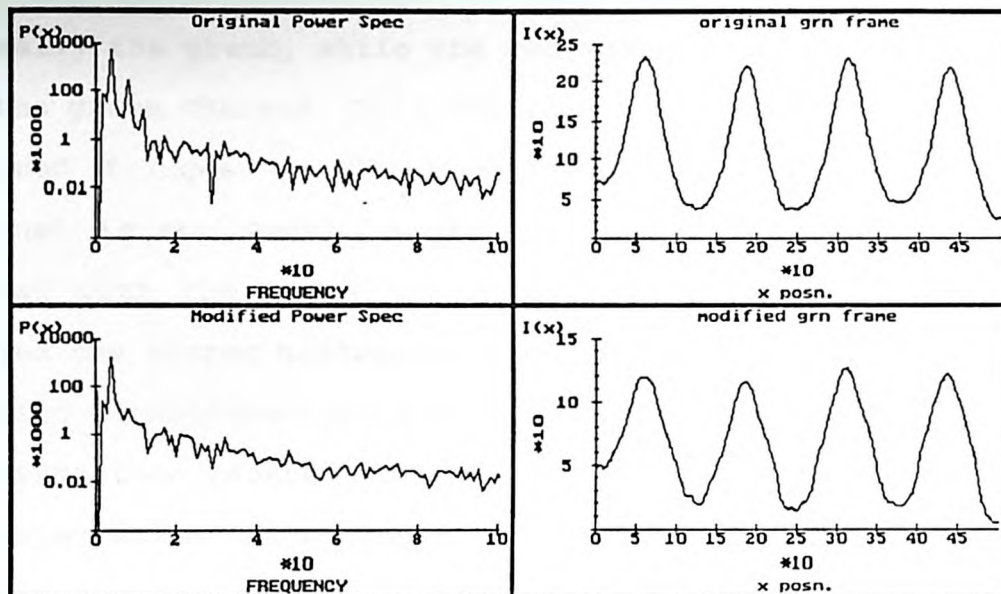


Figure 3.4: Sine wave with and without gamma correction.

Figure 3.4 shows the original sine wave without and with gamma correction with their respective spectral power distribution diagram. From the power spectrum it follows that the Signal to Noise ratio is increased from 12 to 22 dB for the first harmonic of the grating frequency.

3.2.2 Spectral Response Calibration

The gamma correction is only applied to one channel, normally the green, while the red and blue signal are modeled to the green channel. This modeling is done by projecting the colored fringes on the reference plane. Since the green channel is our model, a histogram of the green fringes is formed with the gamma correction. This green histogram is called the master histogram. The histogram of the red fringes is also established and through a technique called histogram specification, [Gonzalez and Wintz, 77] a transfer function is computed which transforms the red histogram into that of the master (green) histogram. This process is repeated for the blue channel also. Thus the red and blue fringes will have the same contribution as the green fringes, guaranteeing equal spectral response. Figure 3.5 shows the original and equalized histograms for each of the red, green and blue frame.

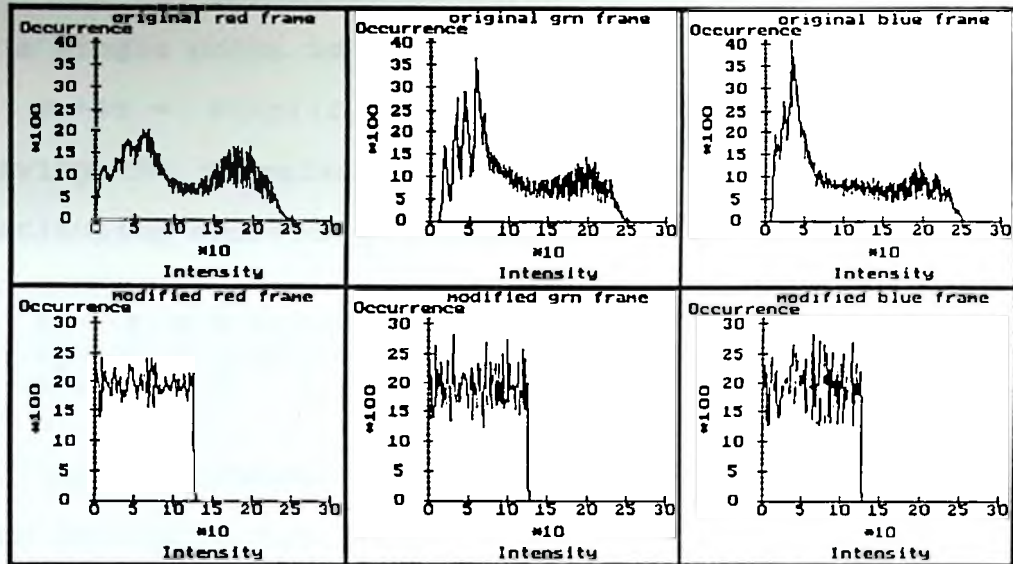


Figure 3.5:Original and equalized histograms.

3.3 Boundary and Gradient Detection

Figure 3.2 showed the calculation procedure to obtain $\phi_r + \phi_z$. In this section it will be shown that it is very simple with this procedure to determine if a data point is valid or must be regarded as noise. A method will be presented to compute the displacement z from this phase plot. Furthermore it will be shown that besides having a limit for the maximum allowed discontinuity there is also a limit for the maximum allowable surface gradient.

Phase plot computation and boundary detection:

With the procedure of [Wyant *et al*, 83] the phase shift for a single point is calculated as:

$$\phi_r + \phi_z = \text{atan}((I_r - I_g) / (I_g - I_b)) \quad [3.4]$$

Deriving the denominator and numerator of this equation by substituting equation 3.1 leads to:

$$\begin{aligned} I_r - I_g &= E b(x,y) \sqrt{2} \cos(\phi_r + \phi_z) \\ I_g - I_b &= (-)E b(x,y) \sqrt{2} \sin(\phi_r + \phi_z) \\ \text{assuming } E_r &= E_g = E_b = E \end{aligned}$$

The two functions are shown in Figure 3.6. From this plot it follows that the denominator and numerator of equation 3.4 are never zero at the same time. This fact can be used to determine if a spatial point contains geometrical data or noise

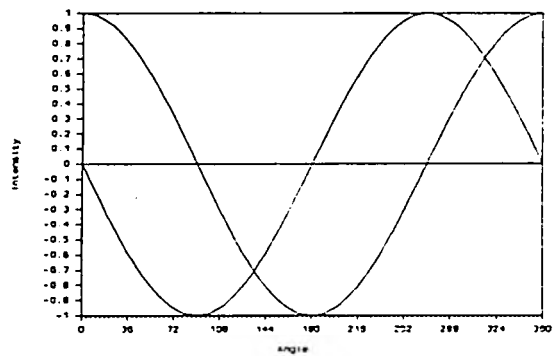


Figure 3.6: Function of computed difference signals.

by checking if the two signals are close to zero. If both signals are both close to zero, the signal can be regarded as noise. Since the two difference signals function as an address pointer into a look-up table, it is a simple manner of assuming a threshold value when the look-up table is

computed and putting a flag at the computed location. In this way the boundary of an object is easily detected since the background of the object is out of focus and contains no geometrical information thus the difference signals of red green and blue are within the threshold.

Unwrapping the phase plot:

The phase plot computed wraps around every 360 degrees. Thus to compute the actual phase shift, the discontinuities must be unwrapped. This is done by scanning a raster scan and computing the gradient of the phase. If the gradient is larger than 180' for example, a discontinuity is assumed and an extra 360' must be added to the phase plot from that point on. The phase unwrapping algorithm used is as described by [Takeda *et al*, 82]. See Insert 3.1 for the algorithm to unwrap a raster scan.

Maximum allowed phase gradient:

To correctly unwrap the phase plot, the discontinuities of the phase plot must be at least three pixels apart. This can be seen from the phase plots shown in Figure 3.7. If the phase plot is defined for only two points, the resulting computed phase shift would always stay zero. Only if the phase plot is defined by at least three points, an actual phase shift can be computed. Although the proof is omitted, it can

```

do
{
  Δφ=φ(xi,Y) - φ(xi-1,Y - φr(xi);
  if(abs(Δφ)>180') then
  begin
    if(Δφ>0)
      wrap=wrap-360'
    else
      wrap=wrap+360'
  end;
  φz(xi)=Δφ+wrap;
  z(xi) = φz(xi)/(2πfg sinθ);
  i=i+1;
}while(i<pixels_in_one_line);

```

Insert 3.1:Unwrap algorithm for a raster scan.

be shown that the requirement for defining the phase plot by at least three points is not only necessary to unwrap the phase properly, but also follows from the sampling theorem.

Since the maximum continuous phase gradient must be equal to or smaller than 120', the maximum profile gradient equals:

$$[dz/dx]_{\max} \leq 1/(3 fg \sin\theta)$$

While unwrapping the phase plot, this condition is checked by confirming that when a discontinuity is detected, the next discontinuity is more than three pixels away.

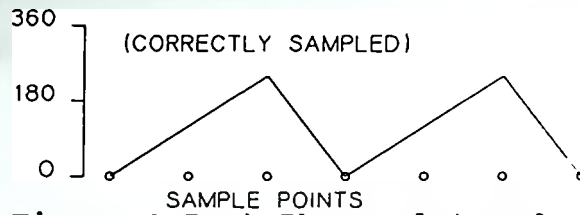
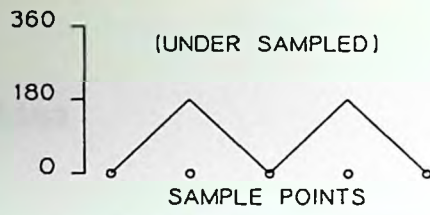


Figure 3.7:a) Phase plot under sampled. b) Phase plot properly sampled.

4.0 System Testing

In this section the test objects used are presented with some comments on their main characteristics. The signal flow of processing one of the objects are to demonstrate the processing steps. The test results and the sources of errors conclude this section.

4.1 Test Objects Selected

To evaluate the practicality of the color fringe projection method, several objects with a wide spread of surface characteristics were examined. See Photo 2 for test objects used. The group of objects shown at the top of the photograph are analytical objects which have a known topography and favourable¹ surface characteristics for color fringe projection. The second group of objects were new and used turbine blades which have a wide range of surface characteristics, varying from a reflective surface when no coating is used on the blade to a black surface area when the turbine blade has been used.

¹Favorable in this context means a white or gray diffuse surface.

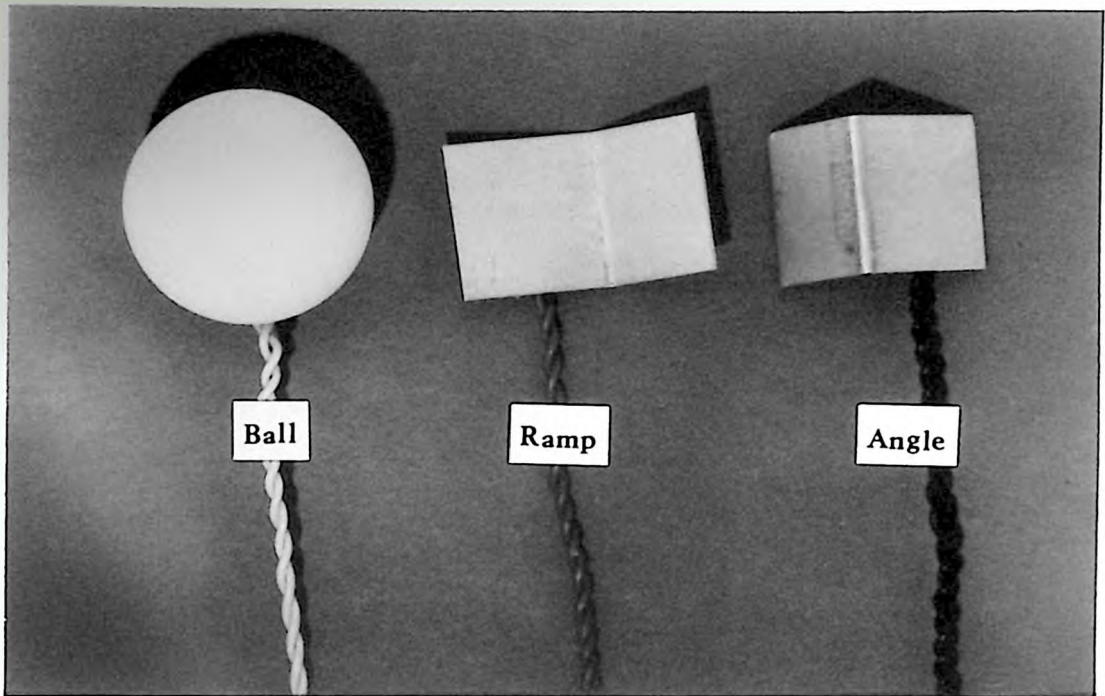
The physical characteristics of the test objects are summarized in Table 4.1.

(Table 4.1 content is extremely faint and illegible)

Table 4.1: Characteristics of test objects.

Object	Material	Color	Size	Surface
Plane under 16' angle	Paper	White	64*64mm	diffuse, covering total view of camera
Ball	Plastic	White	r=19mm	diffuse
Ramp 128'	Aluminum	Gray	38*25mm	Sand Blasted
Angle 90'	Aluminum	Gray	30*25mm	Sand Blasted
Turbine Blade 1	Alloy	Light Gray	45*60mm	Reflecting
Turbine Blade 2	Alloy	Gray	100*200mm	Coated
Turbine Blade 3	Alloy	Black	63*90mm	Used

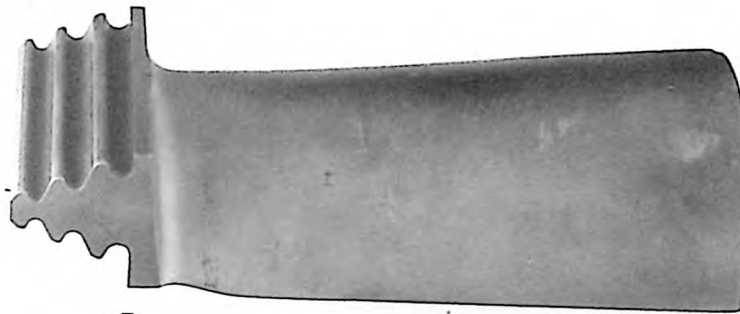
Photo 2: Test Objects



Blade 1



Blade 2



Blade 3



4.2 Processing Example

This section will illustrate the different processing steps followed to obtain the geometrical information of the ball. Photo 3 shows the ball with the color fringes projected on it. Observe that the contour information of the ball is coded into the fringe frequency. Figure 4.1 displays a cross section of the intensity over the center of the ball. The data shown is the intensity as recorded with the 3 chip CCD camera.

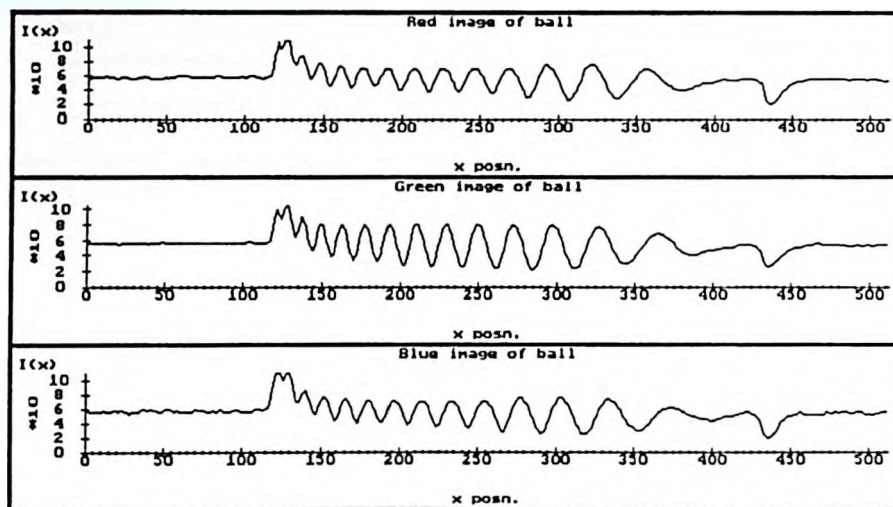


Figure 4.1: Obtained data of ball.

After the intensity distribution of the red, green and blue images are obtained, the difference images are computed. Figure 4.2 shows the computed difference images of the data

presented in Figure 4.1. Notice that by taking the difference of the three color images, the bias $a(x,y)$ which was preset in Figure 4.1 is eliminated. Also note that it is obvious determining if a pixel is part of the ball. If not, the intensity levels of this pixel in the (Red - Green) and the (Green - Blue) image are nearly the same.

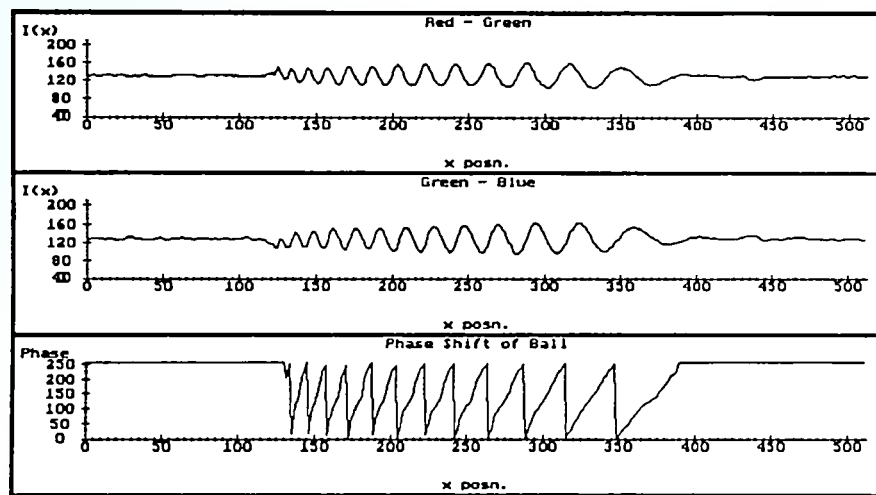
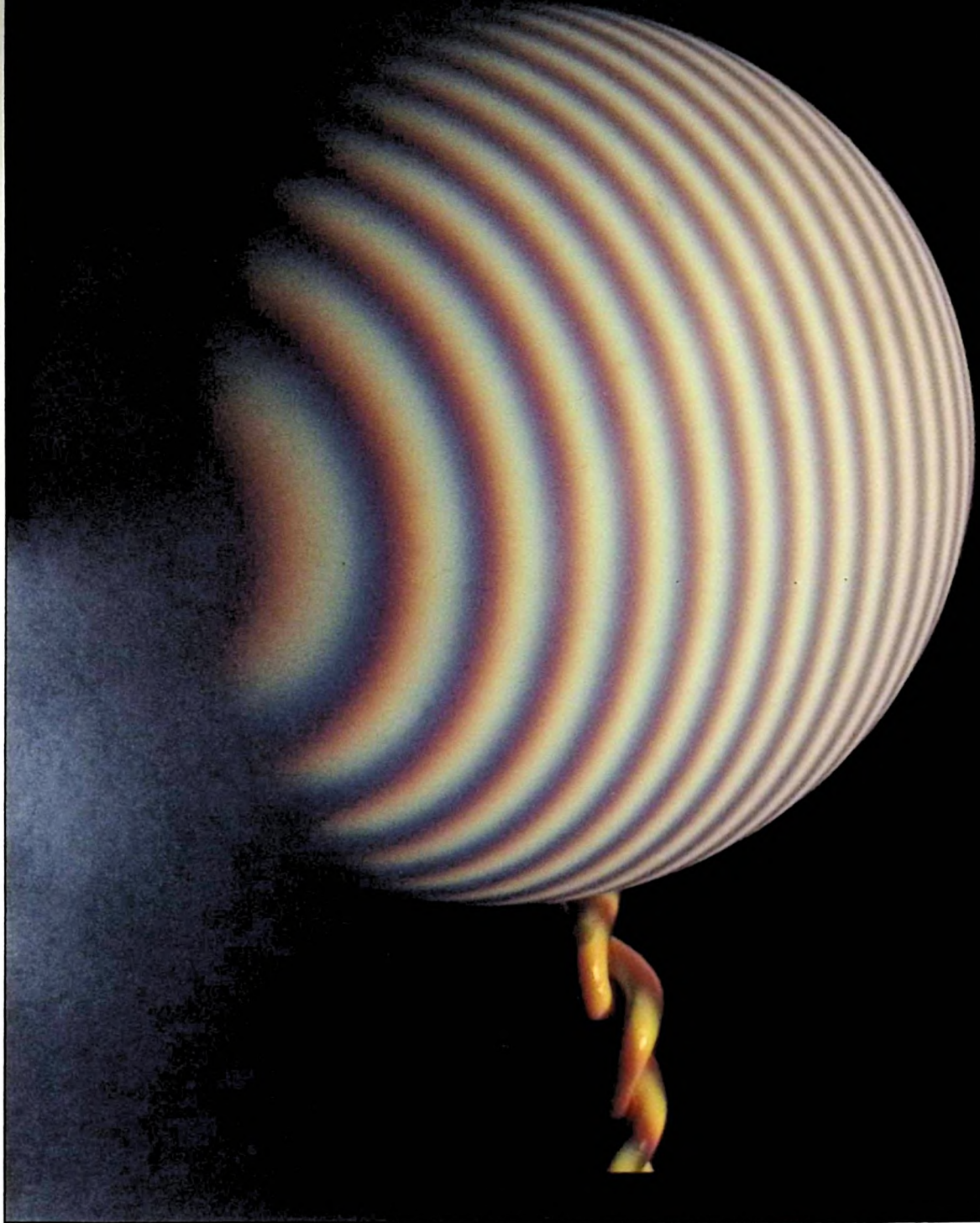


Figure 4.2: Difference and phase plot of ball.

The intensity readings of the (Red - Green) and (Green - Blue) images are now used as an index into a look-up table, which holds the phase information of the given intensity ratio. The computed phase plot is also shown in Figure 4.2.

The phase unwrapping algorithm as proposed by [Takeda *et al*, 82] is used to remove the discontinuities in the phase plot. Since the ϕz is now known, the actual contour is easily computed with the algorithm presented in Insert 3.1. Figure 4.3 shows the contour of the ball.

Photo 3: Color Grating Projected on Ball



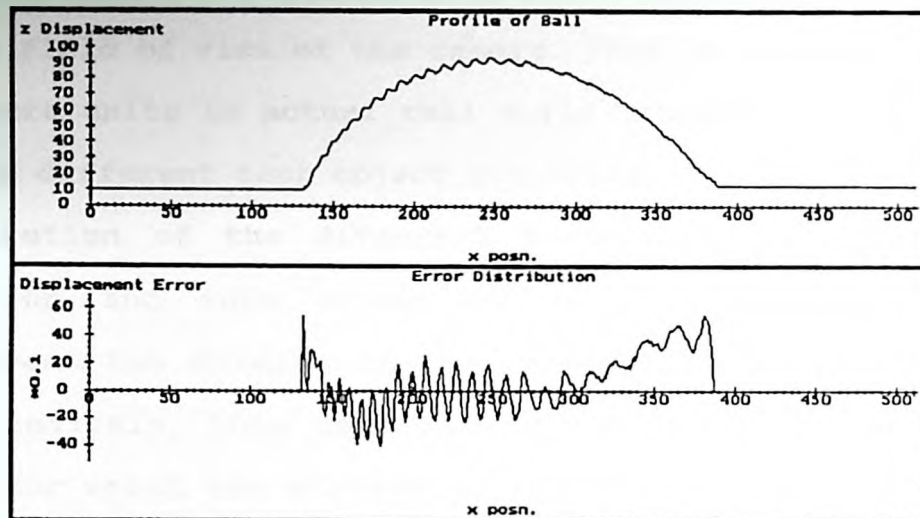


Figure 4.3: Profile of ball and error plot.

Having obtained this contour, an error distribution is generated by comparing it to the analytical contour of the object. This error distribution is also shown in Figure 4.3.

4.3 Experimental Results of Test Objects

In this section the test results of the analytical objects and the turbine blades are presented. The geometrical error distribution of the analytical objects was determined by subtracting the measured profile of the object from the analytical profile. From this error distribution the standard deviation and the mean error was computed and presented.

With the test objects evaluated, the optical magnification was adjusted to obtain an image occupying most of the field of view of the camera. Thus in effect, the ratio of camera units to actual real world dimensions were changed for the different test object evaluated. To compare the error distribution of the different test objects, the standard deviation and mean error are expressed in pixels. To circumvent the dilemma of the optical magnification in the final analysis, this section will conclude by presenting a table for which the standard deviation is normalized to the object dimensions.

Table 4.2 shows the results of the analytical test objects. No filtering or any other type of signal conditioning was done on these objects, with the exception of the 90 degree angle. Due to sources of errors discussed later, it was necessary to put the profile of the 90 degree angle through a median filter to remove noise spikes.

Table 4.2: Error distribution of analytical objects.

Projection angle: $\theta = 30'$

Fringe frequency:
fg = 0.05 cycles per pixel

Scaling: 8 pixels/mm

Plane:
Standard deviation = 0.45 pixels
Average Error = 0.017 pixels

Ramp:
Standard deviation = 0.78 pixels
Average Error = -0.026 pixels

Ball:
Standard deviation = 2.06 pixels
Average Error = 0.661 pixels

Angle:
Standard deviation = 1.27 pixels
Average Error = -0.002 pixels

The evaluation of the turbine blades is done in the same manner, with the exception of deriving the error function. The actual profile of the turbine blades is obtained by fitting a spline through the measured profile of the turbine blade, defined by six points. The error function is then assumed to be the difference of the actual measured profile and the estimated profile. This approach is required since the manufacturing drawings of the turbine blades are not available.

Table 4.3 show the test results of the turbine blades. Also with the turbine blades, no filtering or any other type of signal conditioning was performed. The exception in this case is for turbine blade 3 which due to its black surface needed to be conditioned in two ways. The blue wave front needed to be filtered to remove a low frequency intensity modulation. This was done by passing the blue image through a high pass filter. After this operation the profile of the blade was filtered through a median filter to remove the odd noise spike. Figure 4.4 shows a cross section of each turbine blade and its error distribution.

Table 4.3: Error distribution of turbine blades.

Projection angle: $\theta = 30'$

Turbine blade 1:

Fringe frequency: $fg=0.05$ cycles per pixel
Scaling: 8 pixels/mm

Standard deviation = 1.46 pixels
Average Error = -0.53 pixels

Turbine blade 2:

Fringe frequency: $fg=0.08$ cycles per pixel
Scaling : 2.4 pixels/mm

Standard deviation = 1.13 pixels
Average error = 0.47 pixels

Turbine blade 3:

Fringe frequency: $fg=0.07$ cycles per pixel
Scaling : 5 pixels/mm

Standard deviation = 1.58 pixels
Average error = 0.23 pixels

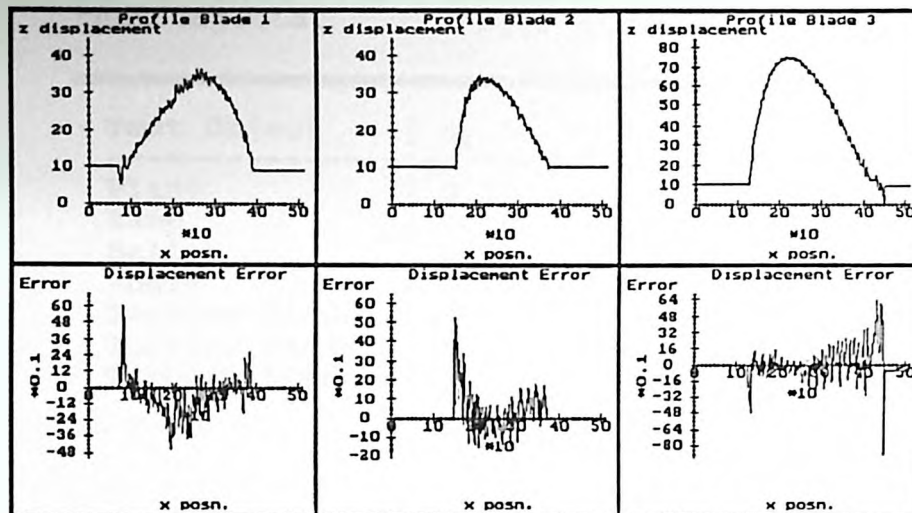


Figure 4.4: Profile and error distribution of turbine blades.

To make a more objective judgement on the accuracy of the Color Fringe Projection method, the standard deviation is also expressed in a relative error w.r.t. to the size of the object. The following formula was used to do this:

$$\sigma_{\%} = \frac{\text{Standard deviation} * 100}{\text{Object size} * \cos\theta * \text{Scaling}}$$

The standard deviation, scaling and the projection angle θ follow from Table 4.2 and 4.3, while the object size follows from Table 4.1. Table 4.4 show the relative standard deviation w.r.t. the object size.

Table 4.4: Relative standard deviation of test objects.

Test Object	σ_x
Plane	0.10
Ramp	0.30
Ball	0.79
Angle	0.61
Turbine Blade 1	0.47
Turbine Blade 2	0.54
Turbine Blade 3	0.58

4.4 Error Evaluation.

From Table 4.4 it follows that 95.5 percent of the readings are well within a relative error of 2 percent.¹ There is, however, still a fair amount of noise present which can be seen from the error distribution plots in Figure 4.3 and 4.4. It was found that this noise is not random since taking an average over multiple contour plots did not improve the standard deviation. The main cause of these errors is most likely due to the limited depth of field and chromatic aberrations of the optical set-up. This can be seen from the

¹Assuming a Gaussian distribution.

error profile of the plane as depicted in Figure 4.5.

The projected fringes are focused in the middle of the plane. However, due to the depth of field of the plane, being under an angle of $16'$, the fringes at the border of the plane are slightly out of focus. This situation also shows up in the error distribution of the plane where it can be seen that the error at the borders is significantly higher than in the middle of the plane.

The breaking index of a lens varies with the wavelength of light. Thus the focal length of a given lens is different for the three primary colors, resulting in different image formations for the red, green and blue image. This distortion is called Chromatic Aberration. Although this chromatic aberration does not help the technique of color fringe projection, it can be compensated for by using achromatic lens systems.

Insert 4.1: Chromatic Aberration.

Other less obvious sources of error are due to the response of the camera used and its supporting electronics. Although no proof will be presented, the following observations were made w.r.t. the camera:

a) The camera was frequency dependent in that the response varied with the grating frequency. It was observed that the distortion of the camera was higher for lower grating frequencies.

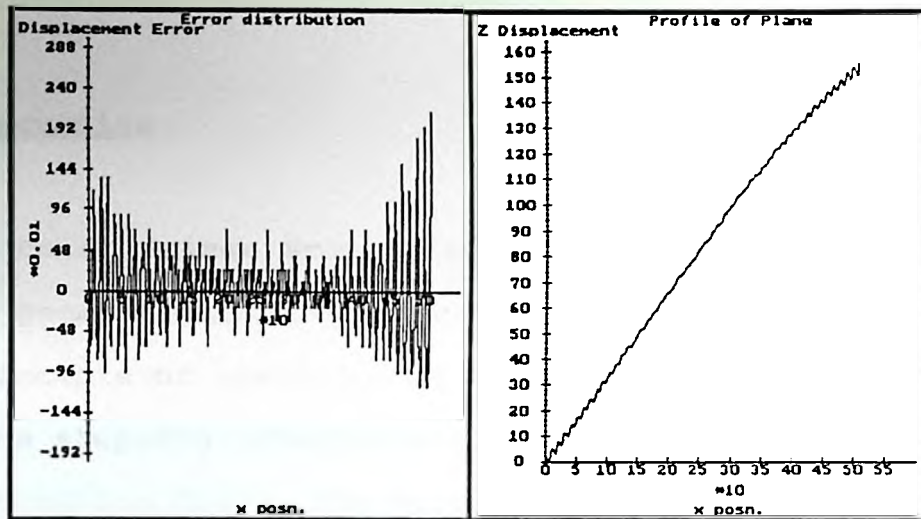


Figure 4.5: Profile and error distribution of plane.

b) Due to "enhancement" circuits in the camera, it showed a certain amount of smear on a raster scan. If for example, a bright object is positioned at the start of a line scan, the intensity of the total line scan is modified.

c) Depending on the white balance of the camera the average dc offset varied significantly for the red, green and blue video signals. The white balance of the camera is an automated calibration circuit which adjusts the red, green and blue video signals to the same amplitude assuming that the camera is looking at a white plane.

5.0 Discussion

A Color Fringe Projection method has been presented to obtain geometrical information from a two dimensional image. The principle of operation of this device is similar to that of phase stepping interferometric designs such as holography and projection Moire. The main difference is that instead of positioning a grating on the object with a servo system, a red, green and blue grating wave front are projected simultaneously onto the surface. With a color camera, these three primary colors are recorded individually and processed in a computer.

The advantages of Color Fringe Projection w.r.t. phase stepping interferometric designs are:

- 1) There is no need for a servo system, thus simplifying the optical set-up.
- 2) Since the three wave fronts are known simultaneously, real time processing can be performed.

5.1 Conclusions

The practicality of this system was evaluated w.r.t. accuracy and sensitivity to the color of the object. The test results show that the color fringe projection can be applied in certain industrial application where one wants to determine the profile of diffuse surfaces with a neutral (gray) color.

It must be noted that the intention of doing these tests was to determine if further research into fringe projection is justified. From the test results one can conclude that it is indeed worthwhile to develop the technique further. The following suggestions serve as a platform to improve the color fringe projection technique.

5.2 Suggestions for Further Research

The set-up of the Color Fringe Projection method was made up of standard commercial components meant for human use only. The needs for machine vision applications are quite different than that of human perception, thus improvements can be made by tuning the equipment to the needs of machine vision. In the following section we will review these needs w.r.t. Color Fringe Projection and in which direction to look for further

improvements.

Projection system:

A commercial slide projector was used to project the slide on the object. These projectors are designed for viewing by the human eye and in no way stand up to the image quality one expects for technical applications. Far a better imaging systems are available such as those used in the fabrication of integrated circuit masks such as projection photolithography.

Image sensor:

For the imaging system (camera) the same restriction applies as for the projector, it is designed for human viewing only. For the human observer the non-linear response of the camera has little effect on the image formation, but when one wants to measure the actual intensities on the object this non-linear response must be compensated for. In this thesis a calibration procedure was suggested to compensate for the non-linear response of the camera, but this compensation is only valid for a fixed

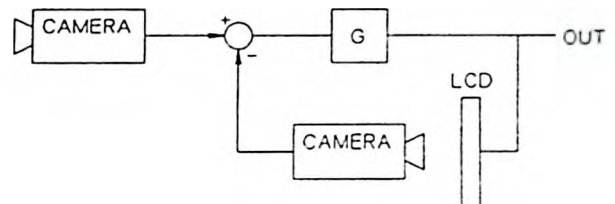


Figure 5.1: Television-optical operational amplifier.

lighting condition.

A more advanced method would be to compensate for the non-linear response of the camera by optical feedback. [Goetz *et al*, 79] suggested this method, as shown in Figure 5.1. From systems theory it follows that if the gain of the amplifier is high enough, the image error will reduce to zero. The major difficulty with this set-up is that the optical transfer function of the two lens systems must be identical.

Frame grabber:

To obtain an overall equal spectral response, it is necessary to adjust the gain and offset of the video signals. In this thesis external hardware was built to accomplish this. However, the electronics of this device can be improved by integrating the gain and offset control into the analog to digital conversion. [Brooktree, 1989] introduced color frame grabber IC's with gain and offset control on-chip under software control. It is suggested to design a frame grabber based on this technology.

2
7
0
2

Appendix I: Holography

This appendix will discuss the mathematical formulation of a holographic recording. To get a more detailed discussion on this matter, the reader should consult introductory books on optics such as [Pedrotti *et al*, 87] or [Meyer-Arendt, 84]. The notation and discussion of holography in this appendix follows, in general, that of Pedrotti.

Figure I,i shows one of the most known hologram recording techniques. A hologram is produced by letting a reference and object wave interfere on a recording medium which is placed under a known angle.

The holographic recording is produced due to the superposition of two light waves, namely, the reference and object wave.

The object wave can be expressed as:

$$E_s = s e^{j\omega t + \phi z}$$

Where:

- E_s = object wave distribution
- s = amplitude of reflected wave front
- ω = $2\pi/T$; T period time of wave
- ϕz = geometric information of object point (x,y)

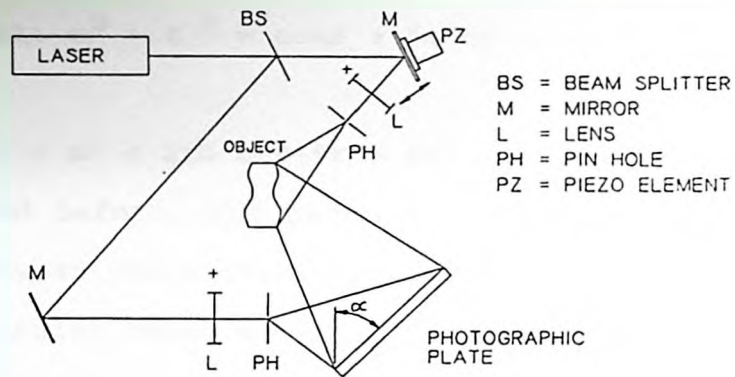


Figure I.i:Holographic recording set-up.

While the reference wave equals:

$$E_r = r e^{j\omega t + j\phi_r}$$

Where:

- E_r = reference wave distribution
- r = amplitude of laser source
- $\omega = 2\pi T$; T period time of wave
- ϕ_r = phase shift due to angle α

On the recording medium, the amplitude equals:

$$E_f = E_r + E_s$$

Knowing that the recorded intensity is proportional to the square of the amplitude, the intensity is computed by multiplying E_f by its complex conjugate E_f^* ,

so that:

$$I = |E_f|^2 = (E_r + E_s)(E_r^* + E_s^*)$$

2
7
0
2

$$I = E_r E_r^* + E_s E_s^* + E_r E_s^* + E_s E_r^*$$

$$I = r^2 + s^2 + rs e^{j(\phi_r - \phi_s)} + rs e^{-j(\phi_r - \phi_s)}$$

Knowing that: $e^{j\beta} + e^{-j\beta} = \cos\beta + j\sin\beta + \cos\beta - j\sin\beta = 2\cos\beta$
 thus:

$$I = r^2 + s^2 + 2rs \cos(\phi_r - \phi_s)$$

As mentioned before, the phase shift ϕ_r is a result of the angle α between the reference wave and the recording plane. This phase shift comes about since the rays as shown in the Figure I,ii meet the film plane later as x is increased.

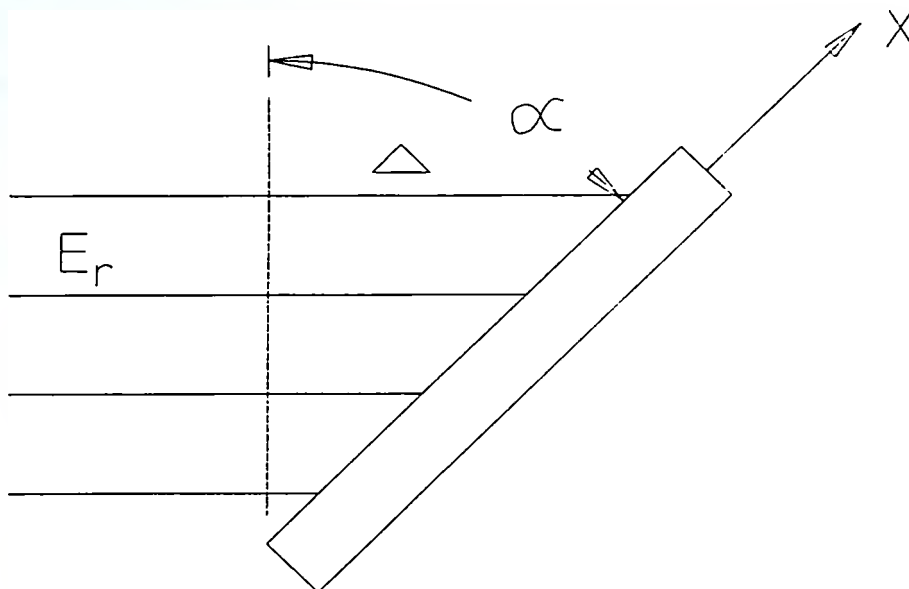


Figure I.ii: Off-axis reference beam formation.

The phase shift can now be expressed as:

$$\begin{aligned} \phi_r &= (2\pi/\lambda)\Delta \\ &= (2\pi/\lambda) x \sin\alpha \end{aligned}$$

A similar expression can be found for ϕz as:

$$\phi z = (-) (2\pi/\lambda) 2z$$

The displacement z shows up as $2z$ since the light wave travels this distance two times, traveling toward it and then back.

What the intensity distribution shows us is that on the recording medium bright and dark fringes will occur due to the phase shift ϕr . Assuming ϕz zero, the intensity will be maximum for ϕr being 0 and π and minimum when ϕr equals $\pi/2$ or $3\pi/2$. It follows that when ϕz is not zero, the resulting fringes on the recording medium are phase modulated by ϕz .

Normalizing the amplitude r and s to the irradiance of the laser gives:

$$r = \beta_r E$$

$$s = \beta_s E$$

Where β_r and β_s^1 are the reflectivity and transmission of the beam splitter with $0 \leq (\beta_r + \beta_s) \leq 1$.

Recognizing that the intensity is a function of space, the recorded intensity can now be expressed as:

¹In practice the surface characteristics of the object are included in β_s . In which case it becomes a function of space.

2
7
0
2

$$I(x,y) = E^2 [a(x,y) + b(x,y) \cos(\phi_r + \phi_z + \delta)]$$

Where:

- I(x,y) = recorded intensity
- E = irradiance energy of laser
- $a(x,y) = (\beta_r^2 + \beta_s^2)$
- $b(x,y) = \beta_r \beta_s$
- $\phi_r = 2\pi/\lambda \times \sin\alpha$
- $\phi_z = 2\pi/\lambda \ 2z$
- λ = wavelength of laser light
- α = tilt of recording medium w.r.t reference beam
- δ = introduced phase shift

The phase shift δ can be introduced by adjusting the optical path length of the reference or object wave. With this adjustment the fringes can be moved on the recording medium, which has certain advantages as explained in Chapter 2.

2
7
0
2

Appendix II: Heterodyne Interferometry

Figure II,i shows the optical set-up for heterodyne interferometry. With the use of Acoustic Optical Modulators, (AOM), the frequency of the laser wave w.r.t. time is modulated with a frequency shift dependent on the AOM. As a result, the fringes of the interferogram are "running" over the surface. The mathematical proof will be given in this appendix.

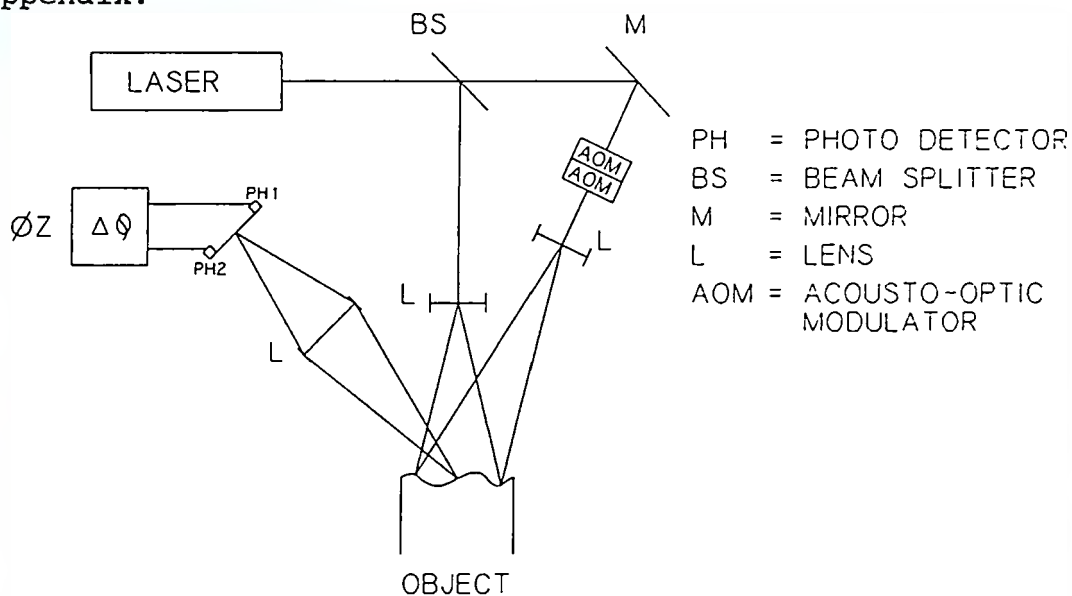


Figure II.i:Heterodyne optical set-up.

The two interfering laser beams can be expressed as:

$$E_1 = \beta_1 E e^{j((\omega + \Delta\omega)t + \phi_1)}$$

$$E_2 = \beta_2 E e^{j(\omega t + \phi_2)}$$

where:

E = proportional with laser amplitude

E_1, E_2 = laser amplitude of beam 1 & 2

β_1, β_2 = reflectivity and transmission of beam splitter, also including surface characteristics of object.

ω = $2\pi/T$

$\Delta\omega$ = frequency modulation introduced in AOM

T = period time of laser wave

$\phi_1 = 2\pi/\lambda \Delta_1$

$\phi_2 = 2\pi/\lambda \Delta_2$

λ = wavelength of laser wave

Δ = distance traveled by laser wave

The observed intensity on the surface of the object equals:

$$I = (E_1 + E_2)^2$$

$$= (E_1 + E_2)(E_1^* + E_2^*)$$

$$= E^2 [\beta_1^2 + \beta_2^2 + 2\beta_1\beta_2 \cos(\Delta\omega t + \phi_1 - \phi_2)]$$

The term $\Delta\omega t$ will cause the intensity to fluctuate in a simple harmonic function, with a beat of $\Delta\omega$. By now comparing the intensities at two pixel locations, it is possible to determine the phase shift between the two pixel positions. This method is shown in the Figure with the two photo diodes.

Assuming that the output of the photo diodes is going through a bandpass filter centered around $\Delta\omega$ the signals obtained are:

$$I_{\text{ref}} = E^2 b_{\text{ref}} \cos(\Delta\omega t + \Delta\Phi)$$

$$I(x,y) = E^2 b(x,y) \cos(\Delta\omega t + \Delta\Phi + \Phi z)$$

where:

I_{ref} = Intensity recorded at a fixed reference position

b_{ref}

$b(x,y)$ = "constant" depending on surface characteristics

$\Delta\Phi$ = phase shift between two wave fronts E_1 & E_2

Φz = phase shift due to surface contour

The phase shift Φz is now easily found with standard electronic circuits.

1
2
7
0
2

2
7
0
2

Appendix III: Projection Moire and Fringe Projection

In this appendix we will discuss the intensity distribution on a object caused by projecting a sinusoidal grating onto that object. Projecting a sinusoidal grating onto a surface is known as the Fringe Projection Method. When the resulting intensity distribution is observed through a second grating of the same frequency, the Fringe Projection Method is called projection Moire. Also the intensity distribution observed with projection Moire will be discussed in this appendix.

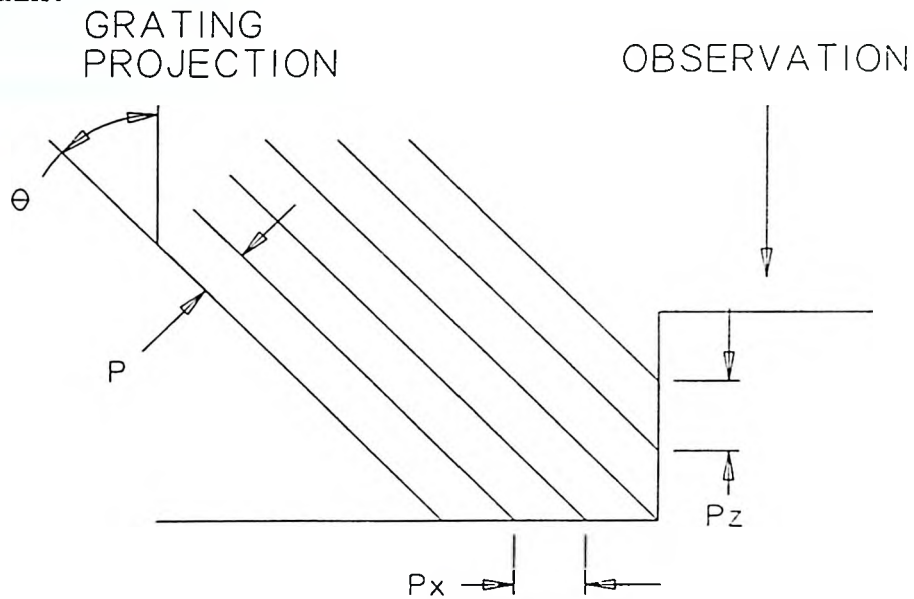


Figure III.i: Fringe projection on surface.

Assuming an optical set-up as shown in Figure III.i, one can conclude that given a projection angle θ and a period p of the original grating, the projected period on the surface of the object w.r.t. the x axis equals:

$$p_x = p \cos\theta$$

Thus the intensity distribution w.r.t. the x axis equals:

$$\phi_r = x \cdot 2\pi/p_x$$

In a similar way the projected frequency w.r.t. the z axis equals:

$$p_z = p \sin\theta$$

and

$$\phi_z = z \cdot 2\pi/p_z$$

Realizing that the projection system modulates the slide containing the grating on the irradiance of the projection bulb, the intensity seen on the surface of the object equals:

$$I(x,y) = E^2 [a(x,y) + b(x,y) \cos(\phi_r + \phi_z)]$$

Where:

- $I(x,y)$ = Intensity at spatial point x,y
- E = proportional to amplitude of light
- $a(x,y)$ = irradiance constant of surface $0 \leq a(x,y) \leq 1$
- $b(x,y)$ = grating visibility on surface $0 \leq b(x,y) \leq 1$
- ϕ_r = $2\pi/p \cdot x \cos\theta$
- ϕ_z = $2\pi/p \cdot z \sin\theta$
- θ = projection angle
- p = grating period

If one observes the projected grating through a second grating of the same frequency as shown in the Figure III,ii, the recorded intensity is the product of the two transmittance functions of the projecting and recording grating. Assuming the transmittance functions to be:

$$T_p = E [a(x,y) + b(x,y) \cos(\phi_r + \phi_z + \delta p)]$$

$$T_r = E [1 + \cos(\phi_r + \delta r)]$$

Where:

T_p = Transmittance function of projected grating

T_r = Transmittance function of recording grating

E = proportional to amplitude of light

$a(x,y)$ = irradiance constant of surface $0 \leq a(x,y) \leq 1$

$b(x,y)$ = grating visibility on surface $0 \leq b(x,y) \leq 1$

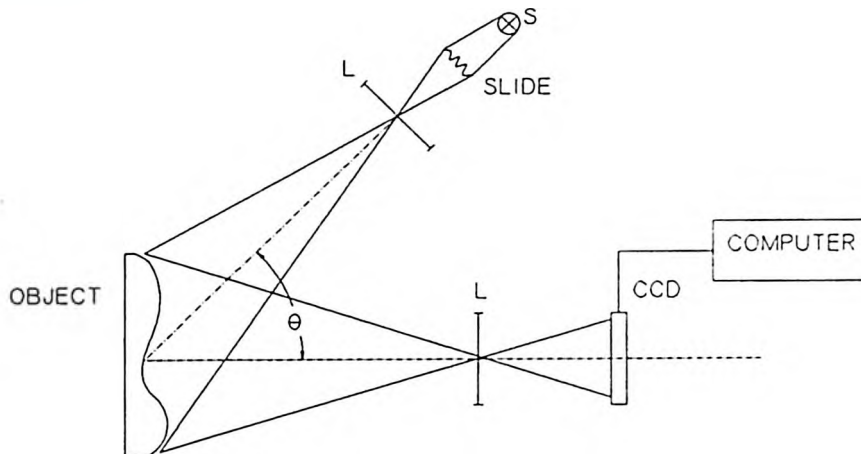
ϕ_r = $2\pi/p \times \cos\theta$

ϕ_z = $2\pi/p \times z \sin\theta$

θ = projection angle

p = grating period

$\delta p, \delta r$ = Introduced phase shift



L = LENS

CCD = CHARGED COUPLED
DEVICE (IMAGE SENSOR)

S = LIGHT SOURCE

Figure III.ii: Projection Moire set-up.

The recorded intensity equals:

$$\begin{aligned} I(x,y) &= T_p T_r \\ &= E^2 [a(x,y) + a(x,y)\cos(\phi r + \delta r) + \\ &\quad b(x,y)\cos(\phi r + \phi z + \delta p) + \\ &\quad \frac{1}{2}b(x,y)\cos(2\phi r + \phi z + \delta p + \delta r) + \\ &\quad \frac{1}{2}b(x,y)\cos(\phi z + \delta p - \delta r)] \end{aligned}$$

From this intensity distribution for Projection Moire one can see that the last term contains the required phase shift ϕz , but this data is obscured due to the higher frequency terms in the intensity distribution. In practice these higher frequency terms are filtered out by slightly de-focussing the recorded image.

11
2
7
10
2

Appendix IV: Fringe Shapes of Michelson Interferometer

In this appendix the grating formation of a Michelson Interferometer will be discussed. By understanding the grating formation, the shape of the fringes can be shown.

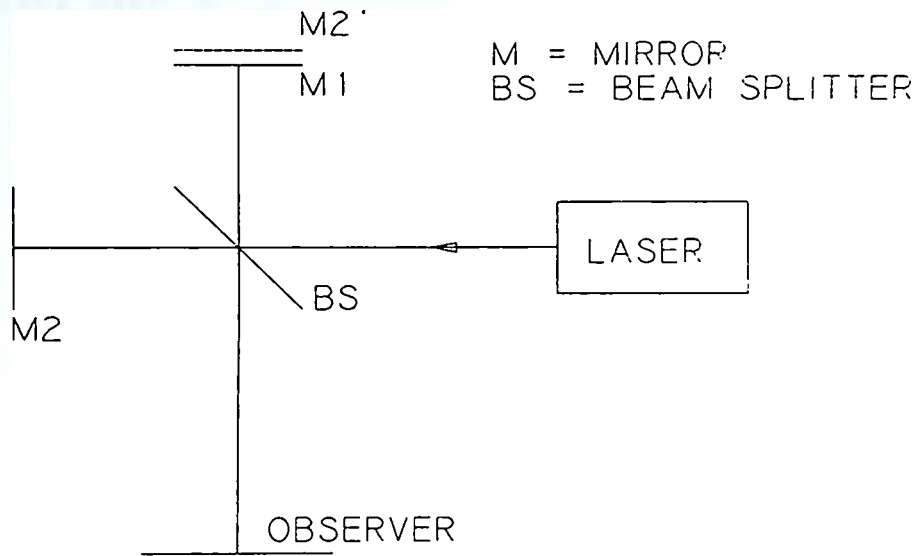


Figure IV.i: Principle set-up of Michelson Interferometer.

Figure IV.i shows the principle set-up of a Michelson Interferometer. For the observer, looking into the Interferometer from O, the mirror M2 appears to be at position M2'. The light reaching the observer, coming from the two mirrors are:

$$E_1 = \beta_1 E e^{j\omega s_1}$$

$$E_2 = \beta_2 E e^{j\omega s_2}$$

Where:

E_1, E_2 = light amplitude from mirror 1 and 2 respectively

β_1, β_2 = reflectivity and transmission of beamsplitter

s_1, s_2 = distance of mirrors to observer

$\omega = 2\pi/\lambda$; with λ wavelength of light source

From the previous appendices, it should be clear that the intensity seen by the observer is proportional to:

$$I \equiv \cos(2\pi/\lambda \ 2d); \text{ with } d=s_2 - s_1$$

A maximum will occur each $2\pi k$ times, thus:

$$2d = k\lambda; \quad k=0,1,2,\dots$$

which is known as the *Michelson Interferometer equation*. From this equation, we will determine the shape of the fringes. The following description has been adapted from [Tolansky, 55].

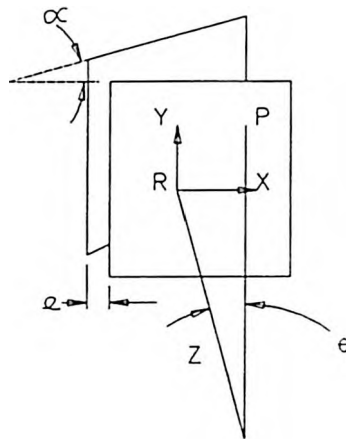


Figure IV.ii: Rays coming from Mirror M1 and M2'.

Figure IV.ii shows the two mirrors and the position of the observer in more detail. An angle α between the mirrors is also introduced. Let the observer be at O, and let R be the foot of the perpendicular from O onto the plane M1. The effect on O of rays coming from point P equals: (Using Michelson Interferometer equation)

$$k\lambda = 2d \cos\theta$$

With d being the separation of the two mirrors at P. The term $\cos\theta$ is introduced since the distance between mirror M1 and M2 apparently is reduced due to the observation angle.

Since:

$$OP^2 = (x^2 + y^2 + z^2)$$

then:

$$\cos\theta = z/\sqrt{(x^2 + y^2 + z^2)}$$

If the spacing at R is e, at P it equals then $(e + x \tan\alpha)$.

Thus for a fringe, k, we can write:

$$2d \cos\theta = k\lambda = 2z(e + x \tan\alpha)/\sqrt{(x^2 + y^2 + z^2)}$$

This expression governs the shape of the fringes.

Straight Fringes:

Assuming e to be zero and z large compared with x and y, then the fringe equation is approximated by:

$$k\lambda = 2x \tan\alpha$$

For a small angle α we can write $\alpha = \tan \alpha$ thus:

$$k\lambda = 2\alpha x$$

This is the equation for a straight line where the fringes are equidistant, separated by a distance $\lambda/2\alpha$.

Circular Fringes:

Assume the angle α to be zero, then the fringe equation becomes:

$$k\lambda = 2ez/\sqrt{(x^2 + y^2 + z^2)}$$

Squaring this, gives:

$$(x^2 + y^2 + z^2) = 4e^2 z^2 / k^2 \lambda^2$$

or:

$$x^2 + y^2 = [(4e^2 - k^2 \lambda^2) / k^2 \lambda^2] z^2$$

For the observer, z is constant, thus $x^2 + y^2$ is constant, which is the equation of a circle. The fringes are thus circles with a radius of:

$$r = (z/k\lambda) \sqrt{(4e^2 - k^2 \lambda^2)}$$

2
12
37
70

2

12
17
10
2

Appendix V: Equipment Used

Projector: KODAK CAROUSEL 750

Projector Lens: KODAK PROJECTION EKTANAR LENS 3 INCH f:3.5

Camera: PANASONIC 300 CLE CCD III MODEL WV-F300

Camera Control Unit: PANASONIC WV-RC36

Camera Lens: STANDARD LENS (J12X10BKRSM)

Frame Grabber: DATA TRANSLATION DT2853 512*480 (8 bits)
(WITH SQUARE PIXEL OPTION)

I/O Board: DATA TRANSLATIONS DT2801

Computer: IBM-AT

Programming Environment: TURBO-C version 2 (Borland International)

Slides produced with a Imapro Inc. PCR film recorder on Ektachrome 100.

11
12
37
90
2

References

[Besl, 88], Active, Optical Range Imaging Sensors. Machine Vision and Applications January (1988) pg 127-152

[Boyer and Kak, 87], Color-Encoded Structured Light for Rapid Active Ranging. IEEE Transactions on Pattern Analysis and Machine Intelligence. January (1987) Vol. PAMI-9, No.1 pg 14-28

[Brooktree Corp.], Bt253 Color Image Digitizer (1989), 9950 Barnes Canyon Rd. San Diego, CA 92121.

[Dessus and Leblanc, 73], The 'fringe method' and its application to the measurement of deformations, vibrations, contour lines and differences of objects. Opto-electronics 5 (1973) pg 369-391

[Goetz, Häusler and Sesselmann, 79], Television-optical operational amplifier. Applied Optics August (1979) Vol.18 No.16 pg 2754-2759

[Gonzalez and Wintz, 77], Digital Image Processing. Addison-Wesley Publishing Company (1977)

[Goodman, 68], Introduction to Fourier optics. San Francisco McGraw-Hill (1968) McGraw-Hill physical and quantum electronics series.

[Grievenkamp, 84], Generalized data reduction for heterodyne interferometry. Optical Engineering July-August (1984) Vol.23 No.4 pg 350-352

[Halioua, Krishnamurthy, Liu and Chiang, 83], Projection moire with moving gratings for automated 3-D topography. Applied Optics March (1983) Vol.22 No.6 pg 850-855

[Hariharan, 85], Optical Interferometry. (1985) Synney: Orlando Academic Press

[Meyer-Arendt, 84], Introduction to Classical and Modern Optics. (1984) Prentice-Hall, Inc., Englewood Cliffs, New Jersey 07632.

u
+2
87
90
12

[Morgan, 82], Least-squares estimation in phase-measurement interferometry. Optics Letters August (1982) Vol.7 No.8 pg 368-370

[Pedrotti and Pedrotti, 87], Introduction To Optics. (1987) Prentice-Hall, Inc., Englewood Cliffs, New Jersey 07632

[Reid, Rixon and Messer, 84], Absolute and comparative measurements of three-dimensional shape by phase measuring moiré topography. Optics and Laser Technology December (1984) pg 315-319

[Sawatari and Zipin, 79], Optical Profile Transducer. Optical Engineering March-April (1979) Vol.18 No.2 pg 222-225

[Takeda, Ina and Kobayashi, 82], Fourier-transform method of fringe-pattern analysis for computer-based topography and interferometry. J.Opt.Soc.Am. January (1982) Vol.72, No.1 pg 156-160

[Thalman and Dändliker, 85], Holographic contouring using electronic phase measurement. Optical Engineering November-December (1985) Vol.24 No.6 pg 930-935

de
:
+2
87
90
.2

mode

7
42
87
90

12

[Tolansky, 55], An introduction to Interferometry. London: Longmans, (1955)

[Walters, 79], Gaging by remote image tracking. Optical Engineering September-October (1979) Vol.18 No.5 pg 473-477

[Womack, 84], Interferometric measurement using spatial synchronous detection. Optical Engineering July-August (1984) Vol.23 No.4 pg 391-395

[Wyant, Koliopoulos, Bhushan and George, 83], An Optical Profilometer for Surface Characterization of Magnetic Media. Proc. 38th Annual Meeting of the ASLE (1983) PREPRINT No. 83-AM-6A-1